Review Article

Nano Research
2021, 14(6): 1668–1681

ISSN 1998-0124 CN 11-5974/O4
https://doi.org/10.1007/s12274-20-3013-4

Substitutional doping in 2D transition metal dichalcogenides

Leyi Loh[1,2,§], Zhepeng Zhang[1,§], Michel Bosman[2] (✉), and Goki Eda[1,3,4] (✉)

[1] *Department of Physics, National University of Singapore, 2 Science Drive 3, Singapore 117551, Singapore*
[2] *Department of Materials Science and Engineering, National University of Singapore, 9 Engineering Drive 1, Singapore 117575, Singapore*
[3] *Department of Chemistry, National University of Singapore, 3 Science Drive 3, Singapore 117543, Singapore*
[4] *Centre for Advanced 2D Materials, National University of Singapore, 2 Science Drive 2, Singapore 117542, Singapore*
[§] *Leyi Loh and Zhepeng Zhang contributed equally to this work.*

Received: 2 June 2020 / **Revised:** 19 July 2020 / **Accepted:** 27 July 2020

ABSTRACT

Two-dimensional (2D) van der Waals transition metal dichalcogenides (TMDs) are a new class of electronic materials offering tremendous opportunities for advanced technologies and fundamental studies. Similar to conventional semiconductors, substitutional doping is key to tailoring their electronic properties and enabling their device applications. Here, we review recent progress in doping methods and understanding of doping effects in group 6 TMDs (MX_2, M = Mo, W; X = S, Se, Te), which are the most widely studied model 2D semiconductor system. Experimental and theoretical studies have shown that a number of different elements can substitute either M or X atoms in these materials and act as n- or p-type dopants. This review will survey the impact of substitutional doping on the electrical and optical properties of these materials, discuss open questions, and provide an outlook for further studies.

KEYWORDS

substitutional doping, transition metal dichalcogenide, two-dimensional semiconductor, acceptor, donor

1 Introduction

Two-dimensional (2D) transition metal dichalcogenides (TMDs) have generated immense interest in the past decade for their rich physics and great potential for novel technological applications [1–3]. Group 6 TMDs have a chemical formula of MX_2 where M represents transition metals (Mo or W) and X represents chalcogens (S, Se, or Te). In the atomically thin monolayer limit, they are direct gap semiconductors [4, 5] with band gaps ranging from near-infrared to visible frequencies. They exhibit considerable room temperature mobility [6, 7], excellent gate electrostatics, and high immunity against short channel effects [8, 9], demonstrating promise for novel electronic applications [10–12]. 2D TMDs are also characterized by their strong light–matter interaction, and their versatile exciton physics makes them attractive for a range of photonic devices such as photodetectors [13–15], light emitting diodes [16–18], and optical modulators [19–21].

The ability to introduce impurity elements and to dope semiconductors with desired carriers is an essential requirement for their practical device implementation. In the past few years, synthesis of various impurity-doped 2D TMDs has been demonstrated by different variations of chemical vapor deposition (CVD) [22–24]. Substitutional impurity doping is significantly more stable as compared to charge transfer doping by surface adsorbates, which are prone to thermal desorption [25–28], and is therefore key to device applications. The basic principle of impurity doping in 2D TMDs is the same as that of conventional compound semiconductors such as GaAs and CdSe. Impurity atoms may substitute either M or X sites and act as donors and acceptors depending on their relative valency (Fig. 1(a)). For example, group 5 (e.g. Nb) and group 7 (e.g. Re) elements substituting M atoms are p- and n-type dopants, respectively, and the same holds true for group 15 (e.g. N) and 17 (e.g. F) elements substituting X atoms. Density functional theory (DFT) calculations show the expected trends for the donor and acceptor energy levels (Fig. 1(b)) [29–33]. Theory [31–37] and experiments [38–42] show that TMDs can host a large number of elements (Fig. 1(c)), and the prospects of dopants such as Co, Fe, and Ni to introduce magnetism in non-magnetic TMD hosts have also generated great interest in recent years [34, 43–45].

As expected, doping of bulk TMDs is known to result in the enhancement of carrier concentration [46–48]. In the monolayer limit, however, the effect of doping is different from that in the bulk, due to reduced screening of Coulomb interaction. Carrier doping is often weak, requiring high impurity densities in the alloying limit before significant conductivity enhancement is observed. Thus, in order to realize the full potential of 2D TMDs, not only the doping chemistry but also the physical effects of impurities need to be thoroughly understood.

In this review article, we provide an overview of the recent developments on substitutional doping of 2D group 6 TMDs and their impact on the physical properties of the materials, such as electrical conductivity and energy band structure. Non-substitutional doping, which has been covered in reviews elsewhere [49–51], will not be discussed here. We start by reviewing the unique effects of monolayer dimensionality, and in Sections 3 and 4, we highlight reports on metal- and chalcogen-site doping including isoelectronic doping where band gap modulation takes place. We will discuss open questions and provide an outlook for future research in Section 5.

Address correspondence to Michel Bosman, msemb@nus.edu.sg; Goki Eda, g.eda@nus.edu.sg

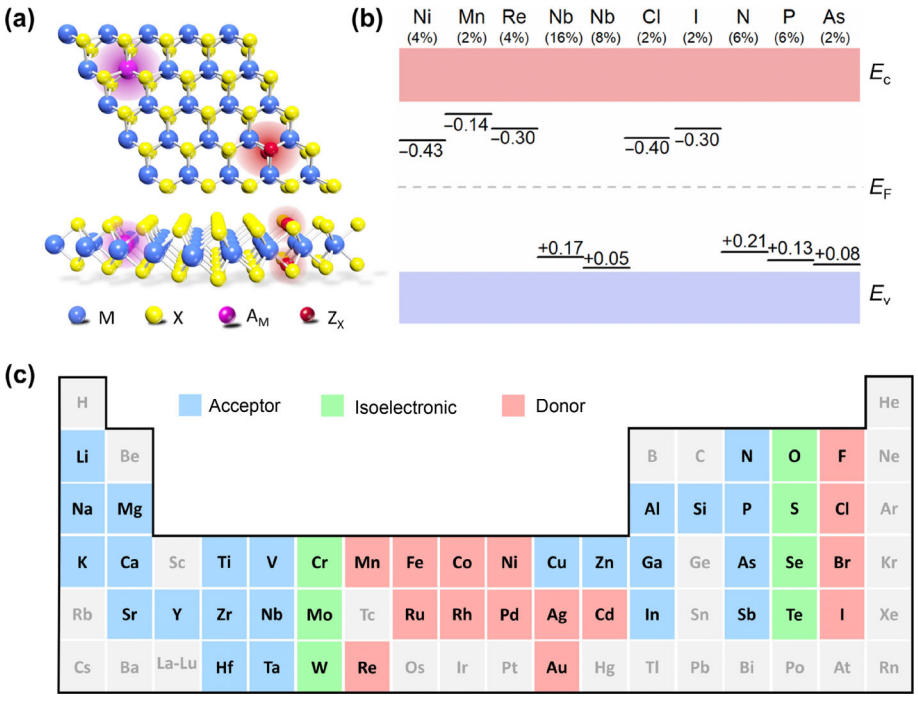

Figure 1 Overview of substitutional doping in 2D group 6 TMDs. (a) Schematic top view (upper panel) and side view (lower panel) of the crystal structure of substitutionally doped monolayer TMD. Blue, yellow, purple, and dark red spheres represent group 6 transition metal (M), chalcogen (X), metal atom (A) substituting M (A_M), and non-metal atom (Z) substituting X (Z_X), respectively. (b) Calculated donor and acceptor energy levels of various substitutional impurities in monolayer MoS_2. The values are extracted from the density of states plots reported in Refs. [29–33]. Doping densities used for the DFT calculations are shown. The values indicate the impurity energy level with respect to the band edge. The horizontal gray dashed line denotes the Fermi level E_F of the undoped material. (c) 45 elements that can substitute M or X atoms in group 6 TMDs [31, 32, 34–42]. Elements shaded in light blue, green and pink are p-type, isoelectronic, and n-type dopants, respectively.

2 Three-dimensional (3D) to 2D semiconductors

When a 3D bulk material is thinned down to the 2D regime, the dielectric screening of Coulomb interaction is greatly reduced. The dielectric constant of monolayer MoS_2 is 4–7.6 [52–54], distinctly lower than the typical values (11–16) of its bulk counterpart [52–55]. As a result, exciton and exciton complexes in 2D TMDs are much more strongly bound compared to those in the bulk [56]. The ionization energy of the dopants is similarly enhanced. The 2D hydrogen model, which is used to describe exciton binding energies, captures this trend [57]. This can be seen as a weak dependence of dopant states to quantum confinement. Due to band gap widening in reduced dimensions [58], the dopant states—with their weak response to quantum confinement—move further away from the band edges, resulting in increased dopant ionization energies [59, 60] (Fig. 2). For comparison, in bulk GaN, Si atoms substituting Ga exhibit an ionization energies between 12 and 17 meV, and for O atoms substituting N, the ionization energy is 34 meV [61]. In bulk Si, the shallow dopants (e.g. As and Sb) have ionization energies of 40–60 meV whereas deep dopants such as In and Tl show ionization energies between 150 and 260 meV [62]. For 2D TMDs, the ionization energies are significantly higher than in bulk semiconductors, in monolayer MoS_2, even shallow-level dopants (e.g. P, Cl, and Br) have ionization energies ranging between 100 and 200 meV [37, 63]. Deep-level dopants (e.g. Na, Nb and Re) in monolayer MoS_2 exhibit an ionization energy of up to 530 meV, resulting in substantially limited carrier activation at room temperature [64, 65].

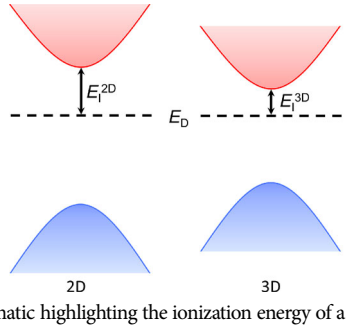

Figure 2 Schematic highlighting the ionization energy of a donor in 2D (left) and 3D (right) semiconductors. Donors require larger ionization energy in a 2D semiconductor than in its 3D counterpart due to the confinement-induced larger band gap and reduced dielectric screening.

Due to the high ionization energy of the dopants in 2D TMDs, the thermal activation rate, which is the number of free carriers per dopant atom at room temperature, is correspondingly small. As a result, to achieve even moderate changes in conductivity, 2D TMDs typically require high doping concen-trations (> 1%), far above the typical ppm- and ppb-level doping used in silicon. For 1% Re-doped MoS_2, the activation rate is reported to be 0.18 [66]. For bulk TMDs on the other hand, the activation rate is several times higher. For example, it is 0.60 for 1% Ta-doped WSe_2 [48]. These differences are summarized in Table 1. It should be noted that the activation rates reported for 2D TMDs are nominal values due to possible impurity band hopping transport [67].

Despite the low activation rate, doped 2D TMDs are expected to be promising for high temperature applications. Due to constant band edge electronic density of states $N(E)$ in 2D systems, the intrinsic carrier concentration is linear in temperature i.e. $n_{i,2D}(T) \propto T$, in contrast to the 3D case where $n_{i,3D}(T) \propto T^{3/2}$. As a result, the intrinsic regime where $n_i(T) >> N_d$ (where N_d is the dopant-derived carrier concentration) appears at a higher temperature in 2D semiconductors compared to 3D semiconductors. 2D TMDs are expected to remain extrinsic ($n_i(T) << N_d$) beyond 1,000 K, distinctly higher than the upper limit of 800 K for silicon [37].

Table 1 Summary of the electronic properties of substitutionally doped 3D and 2D group 6 TMDs[a]

2D/3D	Host	Dopant	Dopant groups	Dopant type	Density (%)	N (cm^{-3} for 3D; cm^{-2} for 2D)	Activation rate	Resistivity (Ω·cm)	Mobility ($cm^2/(V·s)$)	Doping method	References
3D	$MoSe_2$	—	—	—	0	6×10^{16}	—	5	50	CVT	[48]
3D	$MoSe_2$	Ta	5	p	1	6×10^{19}	0.4	2.5×10^{-2}	4	CVT	[48]
3D	$MoSe_2$	Re	7	n	2	4.5×10^{19}	0.15	4.3×10^{-2}	4	CVT	[48]
3D	WSe_2	—	—	—	0	8.0×10^{16}	—	780	99	CVT	[48]
3D	WSe_2	Ta	5	p	0.5	1.6×10^{19}	0.2	30.2	12.9	CVT	[48]
3D	WSe_2	Ta	5	p	1	8.4×10^{19}	0.6	11.7	6.3	CVT	[48]
3D	WSe_2	Ta	5	p	2	2.5×10^{20}	0.9	4.3	5.8	CVT	[48]
3D	WSe_2	Ta	5	p	3	3.5×10^{20}	0.8	3.2	5.6	CVT	[48]
3D	WSe_2	Ta	5	p	5	6.6×10^{20}	0.9	2.5	3.8	CVT	[48]
2D	MoS_2	—	—	—	0	1.5×10^{11}	—	—	18.3	CVD	[66]
2D	MoS_2	Re	7	n	1	2.1×10^{12}	0.18	—	—	CVD	[66]
2D	MoS_2	Mn	7	n	2	2.15×10^{12}*	0.09	—	—	CVD	[69]
2D	MoS_2	Fe	8	n	0.53	1.1×10^{13}	1.80	10^5	50	CVT	[41]
2D	WSe_2	—	—	—	0	—	—	2×10^5*	—	CVD	[86]
2D	WSe_2	V	5	p	1	1.44×10^{12}*	0.13	10^3*	—	CVD	[86]
2D	MoS_2	Nb	5	p	4	—	—	6.5×10^{-2}	—	MOCVD	[67]
2D	MoS_2	Nb	5	p	8	—	—	6.5×10^{-1}	—	MOCVD	[67]
2D	MoS_2	Nb	5	p	11	—	—	6.5×10^{-3}	—	MOCVD	[67]
2D	MoS_2	Nb	5	p	19	4×10^{14}	1.81#	6.5×10^{-4}	1.5	MOCVD	[67]

[a]N: room-temperature carrier density at zero gate voltage. Activation rate: room-temperature carrier density divided by doping density. #: It should be noted that nominal doping density is used to calculate this value. *: The values are extracted from the transfer curves in the references. The equation $N = \varepsilon_{ox} V_{th}/d_{ox}e$ (where the ε_{ox} and d_{ox} are the permittivity and thickness of the oxide layer in the FETs; V_{th} is the threshold voltage; $e = 1.602 \times 10^{-19}$ C) is used to extract the normal state carrier density, which is only applicable in the linear region of the transfer curve across the zero gate voltage.

3 Transition metal substitution

Unlike chalcogen substitution, which can be achieved by post-growth treatment, substitutional metal dopants are typically introduced during material growth. In this section, we will discuss the effects of n-type (e.g. Re and Mn), p-type (e.g. V and Nb), and isoelectronic (W or Mo) doping.

3.1 n-type doping

Re is one of the most commonly reported n-type dopants. CVD growth of Re-doped monolayer MoS_2 is typically achieved using ReO_3 and MoO_3 as precursors [23, 66] but recently, Re doping was achieved by metal-organic CVD (MOCVD) using $Re_2(CO)_{10}$ [67] and liquid-phase CVD with NH_4ReO_4, the ionic analogue of rhenium oxide [24]. The Re atoms are clearly visible in the Mo site from the high Z-contrast in atomic-resolution scanning transmission electron microscope (STEM) images (Fig. 3(a)). STEM imaging offers direct evidence of Re substitution and its random distribution in the host. The actual doping density often ranges between 0.3% and 1% [23, 24, 66]

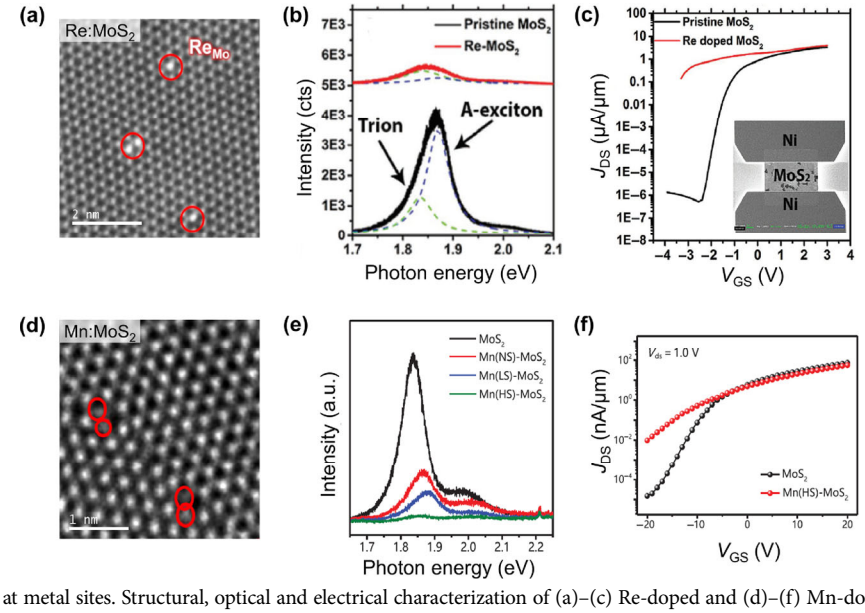

Figure 3 n-type doping at metal sites. Structural, optical and electrical characterization of (a)–(c) Re-doped and (d)–(f) Mn-doped MoS_2. (a) and (d) High angle annular dark field (HAADF)-STEM images showing substitutional impurity atoms. (b) and (e) Room temperature PL spectra of pristine and doped MoS_2. (c) and (f) Transfer characteristics of FETs based on pristine and doped MoS_2. (a) is reprinted with permission from Ref. [24], © American Chemical Society 2020. (b) and (c) are reprinted with permission from Ref. [66], © WILEY-VCH Verlag GmbH & Co. KGaA, Weinheim 2018. (d) is reprinted with permission from Ref. [69], © American Chemical Society 2015. (e) and (f) are reprinted with permission from Ref. [70], © WILEY-VCH Verlag GmbH & Co. KGaA, Weinheim 2019.

but can be as high as 10% [67]. According to DFT calculations, Re forms a donor band ~ 0.1 eV below the conduction band minimum (CBM) in MoS_2 at 1% doping [23]. At this doping concentration, the Fermi level is found to be 0.1 eV below the CBM, based on scanning tunnelling spectroscopy (STS) [66]. Moreover, the electronic band gap was found to be 1.7 eV, significantly smaller than that of an undoped material, which is attributed to the strain induced by Re substitution [66]. The effect of Re doping on the optical properties of the host material varies in the literature. Gao et al. [23] reported a blue shift in photoluminescence (PL) peak energy with no quenching at 0.3% doping, which was shown to be consistent with DFT calculations that predicted an increase in the K-point gap at 1% doping. Zhang et al. [66] on the other hand, reported a redshift in PL with 400-fold quenching and attributed this to increased free carrier concentration (Fig. 3(b)). At 1% doping, the transfer characteristics of MoS_2 show significant negative shift of the threshold voltage with reduced contact resistance [23, 66] (Fig. 3(c)). The device was also shown to exhibit Ohmic behaviour down to 10 K [23]. For $MoSe_2$, high Re doping—or alloying—above 40% resulted in structural phase segregation, with lower Re content regions (~ 23%) showing the 2H phase, and regions richer in Re (> 40%) exhibiting the 1T' phase [68].

Mn has also been explored as an n-dopant. Incorporation of Mn into the lattice of MoS_2 by CVD requires careful optimization of growth conditions. Use of graphene as the substrate [69] and MnO_2/NaCl as dual additives [70] was reported to be critical for efficient incorporation of Mn. Reported doping densities range from 1.1% to 2.4% with most Mn atoms distributed randomly and uniformly in the host, and with some Mn segregation at domain boundaries [69] (Fig. 3(d)). Thermal activation energy of Mn dopants in MoS_2 was extracted to be 120 meV from temperature-dependent conductivity measurements [71]. According to electronic density of states (DOS) calculations, an isolated Mn dopant is shown to form impurity states near the CBM [72]. Similar to Re doping, there is some disparity in the reported impact of Mn doping on the optical and electrical properties of the host material. Zhang et al. [69] observed a redshift in PL while Cai et al. [70] observed a blueshift with increasing Mn content (Fig. 3(e)). The former group found an order of magnitude lower device conductance for 1.1% Mn-doped MoS_2 in the normal state (i.e. $V_{GS} = 0$, where V_{GS} is the gate voltage) compared to the pristine MoS_2 devices, whereas the latter group did not observe any change in the normal state device conductance at 2.4% doping (Fig. 3(f)). Further, a unexpected p-type enhancement was reported for Mn:MoS_2 by Huang et al. [71]. Although these findings appear to disagree, these reports consistently show the absence of the total conductance enhancement, indicating the large ionization energy of the dopants. The reported difference in the conductivity is most likely due to different impurity-mediated hopping parameters rather than free carrier densities [67].

Substitutional Fe doping in MoS_2 has been achieved by chemical vapor transport (CVT) [41] and CVD with solid MoO_3/FeS_2 precursors [73]. Wang et al. [41] estimated the ionization energy to be 68 meV from temperature-dependent conductivity measurements. According to DFT calculations, Fe introduces two impurity states near CBM, that are deeper than that of Mn dopants [74]. Low temperature photocurrent spectroscopy showed the emergence of a peak at 1.2 eV, which can be attributed to the deep Fe level [41]. Li et al. [73] reported a redshift and quenching in the PL of MoS_2 after introducing 2% Fe doping, as quantified under STEM. In contrast, a recent report by Fu et al. [44] showed the emergence of a Fe-derived PL peak above the ground exciton peak in their 0.3%–0.5% Fe-doped MoS_2 monolayer. The material was further found to exhibit room temperature ferromagnetism. Hall measurements indicated that Fe-doped MoS_2 is n-type, with a higher carrier concentration but lower mobility compared to pristine MoS_2 [41].

Higher valency elements such as Co and Cu can also substitutionally dope TMDs but their effects are not widely investigated. To date, high level (> 10%) Cu and Co doping was achieved for WS_2 by CVT [75] and for MoS_2 by CVD, respectively [76]. DFT calculations show that Cu impurity states span over a range of ~ 1 eV in the band gap of WS_2 [77]. For Co-doped MoS_2, the impurity states also span over a similarly wide range, but their average energy is closer to the CBM. It was inferred that impurity bands gradually shift from the CBM to the valence band maximum (VBM) with increasing valency from Mn to Cu such that Cu may also act as a p-type dopant [78]. Bilayer $Co_xMo_{1-x}S_2$ field-effect transistors (FETs) showed n-type characteristics but with no clear evidence of Co-induced carrier doping [76]. Cu-doped WS_2 FETs showed n-type characteristics with 1–3 orders of magnitude lower contact resistance and 5–7 times higher electron mobility as compared to their pristine counterpart. However, the carrier doping was non-degenerate, despite the high Cu content [75].

Since native defects such as chalcogen vacancies are believed to render TMDs n-type, identifying the effect of nominally n-type impurities is challenging, especially given the low activation rate of these dopants. The problem is also complicated by the possible change in the native defect density in modified growth conditions and the physical interaction between the impurities and the native defects [66].

3.2 p-type doping

Nb is a common p-type dopant for TMDs [23, 79, 80]. Nb-doped WS_2 and MoS_2 have been grown by powder CVD using $NbCl_5$ [23, 80], Nb metal [81] and Nb_2O_5 [79] as the Nb source, by CVT using Nb metal [82], and by MOCVD using $NbCl_5$ [67], with achieved doping densities between 1% and 19% [23, 67, 80, 81]. Qin et al. [83] showed that the doping density in their Nb-doped WS_2 grown using liquid phase mixtures decreases from the center to the edge region of the triangular crystals by as much as 50% [84] (Fig. 4(a)). Such a spatial variation was also observed in V-doped WS_2 [85]. Nb dopants introduce an acceptor state in MoS_2 above a doping density of 8% [29, 32, 79]. Similarly, DFT calculations show that 6.25% doping of Nb in WS_2 does not introduce midgap states but brings the Fermi energy below the VBM to maintain the charge neutrality of the system [23]. Experiments have shown that the PL peak redshifts and broadens with increasing Nb content (Fig. 4(b)) but the spectral shapes and peak energies vary among the reports [80, 81, 83]. Jin et al. [80] and Suh et al. [82] observed enhanced electrical conductivity and concluded that the p-type doping is degenerate at Nb content of 1.4% and 0.5%, respectively, based on suppressed gate modulation. Other groups observed reduced normal state conductance [79, 83]. Qin et al. [83] observed a progressive positive shift of the FET threshold voltage and the emergence of a hole branch at Nb content of > 2.5% (Fig. 4(c)).

V has also been shown to act as a p-type dopant. A series of V-doped WSe_2 monolayers with doping concentrations ranging from 0.5% to 20% were synthesized by CVD using $NH_4H_2W_{12}O_{40}$/NH_4VO_3 as metal precursors [86]. The liquid precursors allowed direct growth of V-doped WSe_2 with good spatial uniformity and reasonable control of doping densities (Fig. 4(d)). With the same W liquid precursor and $VO[SO_4]$, Zhang et al. [85] reported the growth of V-doped WS_2 monolayers with V densities ranging from 0.4% to 12% with minimal dopant aggregation. V introduces an acceptor state situated approximately

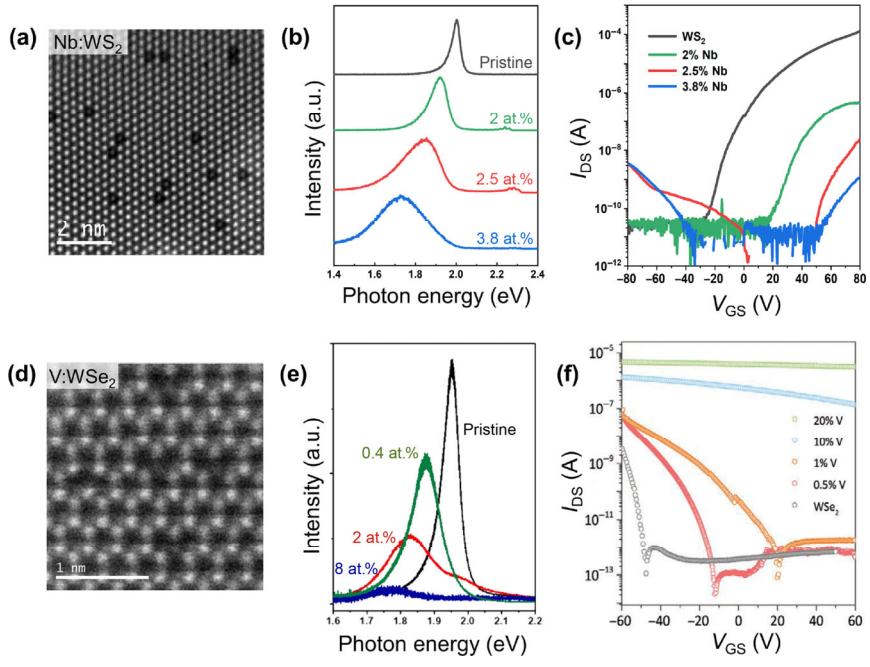

Figure 4 p-type doping at metal sites. Structural, optical and electrical characterization of (a)–(c) Nb-doped WS_2 and (d)–(f) V-doped W(S)Se_2. (a) and (d) HAADF-STEM images showing substitutional impurity atoms. (b) and (e) Room temperature PL spectra of pristine and doped WS_2 with increasing doping concentrations (top to bottom). (c) and (f) Transfer characteristics of FETs based on pristine and doped WS_2 and WSe_2. (a)–(c) are reprinted with permission from Ref. [83], © American Chemical Society 2019. (d) and (f) are reprinted with permission from Ref. [86], © Yun, S. J. et al. 2020. Published by WILEY-VCH Verlag GmbH & Co. KGaA, Weinheim. (e) is reprinted with permission from Ref. [85], © Zhang, F. et al. 2020. arXiv.org e-Print archive.

0.14 eV above the VBM as measured by STS over individual dopants in WSe_2 [87]. Similar to the case of Nb doping, V doping results in red-shifted and quenched PL [85, 86] (Fig. 4(e)). V-doped WSe_2 FETs exhibit increasing hole current with increasing V content, and above 10% dopant concentration, gate modulation is significantly suppressed, suggesting degenerate doping [86] (Fig. 4(f)). Similarly, increasing V-doping in WS_2 monolayers shifts the threshold voltage of the electron branch to more positive gate voltages, accompanied by the gradual emergence of a hole branch, eventually transforming the typically unipolar n-type WS_2 to an ambipolar material at high doping density of 8% [85].

Y and Zr are potential p-type dopants according to DFT calculations. However, no experimental studies have so far been reported. In contrast to Nb, Y and Zr impurity states in MoS_2 are less hybridized with the valence band states and are predicted to form deep acceptor states [32].

An unexpected p-type dopant is Zn. Zn-doped monolayer MoS_2 films have been grown by CVD using MoO_3/ZnS solid precursors. The doping concentration extracted from X-ray photoelectron spectroscopy (XPS) was 1%–2%. According to DFT calculations, Zn introduces several states above the VBM and lowers the Fermi level. Zn-doped MoS_2 FET devices showed reduced n-type character and the emergence of a hole-like branch after sulfur annealing, which is expected to suppress the n-doping arising from sulfur vacancies [39].

3.3 Isoelectronic doping

In conventional compound semiconductors, isoelectronic doping can be employed to suppress native defects such as dislocations, which is the case for In-doped GaAs and Te-doped Sb_2Se_3 [88–91]. The faster migration of In compared to Ga makes In adatoms occupy normally vacant Ga sites during growth, thus reducing the vacancy defect density [92]. The defect-suppressing effect with isoelectronic doping in TMDs is similar to that in conventional semiconductors. Doping $MoSe_2$ with W in alloying concentrations of up to 18% modifies the host band structure and also makes initially deep defect levels of selenium vacancy (V_{Se}) shallower with respect to the CBM [93, 94] (Figs. 5(a) and 5(b)). Introducing 2% W in $MoSe_2$ resulted in V_{Se} reduction by 38%, and a further increase in W content up to 18% resulted in a total V_{Se} reduction of 50% relative to undoped $MoSe_2$ [93]. According to free energy calculations, V_{Se} are predicted to form preferably around W dopants in $Mo_{1-x}W_xSe_2$ alloys where these defect states are promoted closer to the CBM of the alloy. With increasing number of W as nearest neighbours around V_{Se}, the energy difference between the defect states and the CBM can be systematically reduced [94] (Fig. 5(b)), promoting initially deep defect levels to shallower positions in the band gap. The reduced defect density and shallower defect levels manifest as enhanced PL intensity and quenched defect emission [93]. Despite the same valency, W doping renders naturally n-type $MoSe_2$ more p-type (Fig. 5(c)) in character [95]. This is attributed to the larger electron affinity of W compared to Mo as reflected in the enhanced local density of states near the VBM at the W sites. Unlike conventional semiconductors where alloying results in continuous tuning of the band gap known as the bowing effect [96–98], the band gap of $Mo_{1-x}W_xSe_2$ alloys is expected to remain unchanged for W content up to 25% (Figs. 5(d) and 5(e)) [99].

In contrast to the case of $Mo_{1-x}W_xSe$, a study on Mo doping of WS_2 did not find suppression of sulfur vacancy (V_S) defects. However, similar to W in $MoSe_2$, V_S defects have a higher affinity towards Mo in WS_2 host. This affinity between Mo and S vacancies manifests in the splitting of partially-filled defect bands related to V_S due to symmetry breaking when Mo is in the vicinity. According to DFT calculations, the Mo dopant splits the originally degenerate bands into two levels that are 0.15 eV apart in the band gap [100]. Band gap modulation and carrier doping effects of $Mo_{1-x}W_xS$ alloy system remain unexplored.

Cr can occupy different sites in the TMD lattice; M-site substitution is not necessarily the lowest energy configuration [101]. Unlike Mo and W isoelectronic doping where the alloy lattice

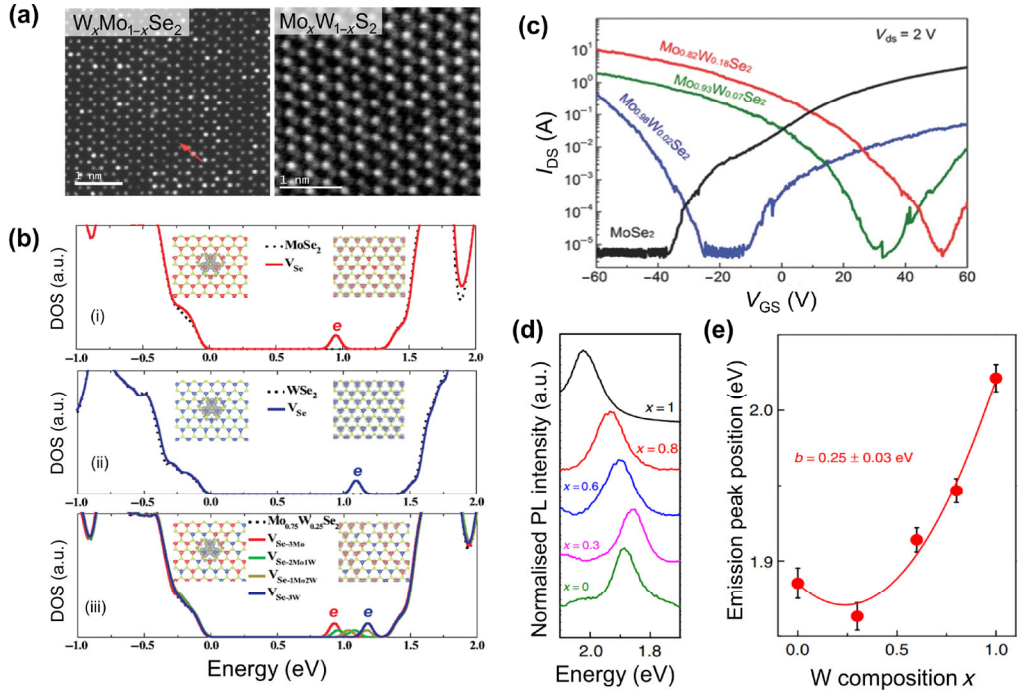

Figure 5 Isoelectronic doping at metal sites. (a) HAADF-STEM images of W-doped $MoSe_2$ (left panel) and Mo-doped WS_2 (right panel). (b) Electronic DOS of (i) $MoSe_2$, (ii) WSe_2, and (iii) $Mo_{0.75}W_{0.25}Se_2$ with (solid line) and without (dashed line) Se vacancies V_{Se}. (c) Transfer curves of FETs based on $MoSe_2$ and $Mo_{1-x}W_xSe_2$ with different W content. (d) PL spectra for $Mo_{1-x}W_xS_2$ monolayer for x = 1, 0.8, 0.6, 0.3 and 0. (e) Plot of PL peak position versus W composition (x). Error bars represent standard deviation of PL peak position in five-times repeatedly synthesized $Mo_{1-x}W_xS_2$. The left panel of (a) is reprinted with permission from Ref. [95], © WILEY-VCH Verlag GmbH & Co. KGaA, Weinheim 2016; the right panel of (a) is reprinted with permission from Ref. [100], © American Chemical Society 2017. (b) is reprinted with permission from Ref. [94], © American Physical Society 2015. (c) is reprinted with permission from Ref. [95], © WILEY-VCH Verlag GmbH & Co. KGaA, Weinheim 2016. (d) and (e) are reprinted with permission from Ref. [99], © Macmillan Publishers Limited 2015.

structure remains hexagonal for all compositions, Cr is reported to induce structural disorder in MoS_2 at 8.6% doping [102]. This is consistent with the fact that chromium sulfides ($CrS_{0.95}$-$CrS_{1.5}$) exist in the trigonal, monoclinic or rhombohedral crystal system [103, 104]. In contrast to the p-type enhancement in $MoSe_2$ by W, the lighter Cr was reported to promote n-type doping in MoS_2 [71]. This n-type enhancement is in line with the first-principles studies that predicted substitutional Cr in WSe_2 to be n-type dopants [105].

4 Chalcogen site substitution

Substitution of chalcogen with impurities can be more conveniently achieved than metal site doping by post-growth processes because chalcogen atoms are exposed at the outer surface of TMDs [49]. Moreover, substitution of the outer chalcogen sites leaves the transition-metal layer nearly undisturbed, ensuring minimal scattering for bands edge charge carriers [37]. According to theoretical predictions, non-metal groups 15, 16 and 17 elements can replace the chalcogen atoms to form a stable ternary TMD phase. Among these groups, pnictogen and halogen elements are identified as suitable p-type and n-type dopants for group 6 TMDs, respectively. N- [106], P- [107] and Cl- [108] doped TMDs have been synthesized via various methods. These doped materials demonstrated tuneable electron densities and showed great potential for low contact resistance transistors [108], high rectification ratio p-n diodes [107], and high responsivity photodetectors [109]. Isoelectronic doping with chalcogen elements does not induce mid-gap states but can continuously shift the band edge states and can correspondingly modulate the bandgap of the doped (or alloyed) material [32]. A variety of ternary alloys $MoS_{2-x}Se_x$ [110], $WS_{2-x}Se_x$ [111], $WSe_{2-x}Te_x$ [112], and $MoS_{2-x}O_x$ [113] have been synthesized by direct CVD and post-growth treatment, and they are found to exhibit continuously tuneable bandgaps and structural phases.

4.1 n-type doping

According to DFT calculations, the formation of pnictogen and halogen dopants in a X-rich (M-poor) environment is energetically unfavourable compared to that in a Mo-rich (X-poor) environment [32]. Typical CVD growth conditions involve a high chalcogen vapor pressure to avoid chalcogen vacancy defects, which is therefore not suitable for the direct synthesis of pnictogen- and halogen-doped TMDs. Nevertheless, a few groups succeeded in the direct growth of Cl-doped MoS_2 by using Cl-rich substrates in CVD, and N-doped MoS_2 by sulfurizing N-rich Mo-based compounds [109, 114]. Alternatively, TMDs with chalcogen vacancies can be intentionally prepared to facilitate the substitution process in a post-synthesis treatment. This is an energetically favourable route to realizing pnictogen and halogen doping and is widely reported. Commonly used post-treatment methods include dopant-rich solvent soaking, gas annealing, and plasma treatment [106–108, 115].

Halogen doping has so far mainly been conducted with Cl. Yang et al. [108] developed a facile way to Cl-dope few-layer (3.5–5 nm) mechanically exfoliated WS_2 and MoS_2, which involves soaking the flakes in undiluted 1,2-dichloroethane (DCE) at room temperature for more than 12 h (Fig. 6(a)). A ~ 0.3 eV blue shift of the core level binding energies of WS_2 was observed after DCE treatment, indicating n-type doping. The observed negative threshold voltage shift for WS_2 FETs after DCE treatment further supported the n-doping effect (Fig. 6(b)). Doping also resulted in a significant reduction of the contact resistance R_c of WS_2 and MoS_2 FET devices from ~ 100 and ~ 6 to 0.7 and 0.5 kΩ·μm, respectively. Moreover, a considerable room temperature FET mobility of 60 $cm^2/(V{\cdot}s)$ was achieved in the treated WS_2 device. Based on the sheet resistance and carrier mobility of the doped MS_2, the Cl doping density in

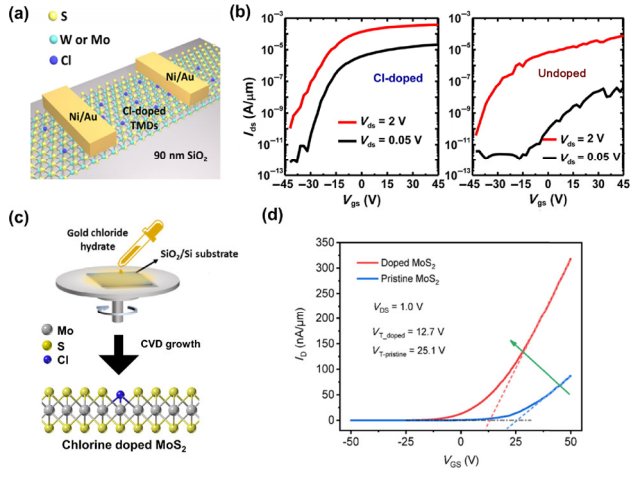

Figure 6 n-type doping at chalcogen sites. (a) Schematic of Cl-doped few-layer TMD FET. (b) Transfer characteristics of Cl-doped (left) and undoped (right) WS_2. (c) Schematic of the gold chloride hydrate pretreatment of Si/SiO_2 substrates (top) and the crystal structures of Cl-doped monolayer MoS_2 (bottom). (d) Transfer characteristics of Cl-doped (red) and undoped (blue) MoS_2 FETs. (a) and (b) are reprinted with permission from Ref. [108], © American Chemical Society 2014. (c) and (d) are reprinted with permission from Ref. [109], © American Chemical Society 2019.

WS_2 and MoS_2 after DCE treatment was estimated to be 6.0×10^{11} and 9.2×10^{12} cm^{-2}, respectively. It is worth noting that the doping density is still lower than the typical sulfur vacancy density in these materials [113], suggesting that the defects are not fully passivated.

Li et al. [109] demonstrated direct growth of single-layer Cl-doped MoS_2 using Cl-rich substrates, which was prepared by heating a SiO_2/Si wafer coated with gold chloride hydrate (Fig. 6(c)). Similar to DCE-treated MS_2 [108], a small negative shift of the threshold voltage was observed in Cl-doped MoS_2 FETs compared to the undoped control devices, indicating successful n-type doping (Fig. 6(d)). Interestingly, the visible light photodetectors made with Cl-doped MoS_2 were found to exhibit high responsivity of 99.9 A/W, which is more than an order of magnitude larger than that of undoped MoS_2. This enhancement was attributed to passivation of substrate-induced electron trap states near the conduction band of MoS_2 by extra carriers introduced by Cl doping. It is worth noting, however, that no clear signature of carrier doping was observed in the PL spectrum of Cl-doped material [109].

While Cl doping was shown to be feasible for MS_2, alternative n-type dopants such as F, Br and I remain experimentally unexplored. It is, however, worth noting that iodine and bromine are commonly used as a transport agent for the CVT growth of bulk TMD crystals. It is thus possible that synthetic TMD crystals are unintentionally doped with these elements. Early studies showed that iodine was found in HfS_2 crystals at density of 10^{15} atoms/cm^3 when 5 mg/cm^3 iodine was used during CVT growth [116]. This density translates to 10^8 atoms/cm^3 in 2D TMDs. It remains to be addressed whether halogen doping at such low densities has impact on the electrical and optical properties of TMDs.

4.2 p-type doping

Pnictogens, while being typical n-type dopants for Si, act as p-type dopants in group 6 TMDs. Pnictogen doping in TMDs has been achieved with N and P, mostly using post-growth treatments including NH_3 plasma treatment [117], N_2 plasma treatment [106], annealing in NH_3 [115], and PH_3 plasma treatment [107]. Alternative bottom-up approaches including sulfurization of WO_xN_y film [114], and sintering Mo-S-N compounds [118] have also been demonstrated.

Azcatl et al. [106] reported that N-doping of MoS_2 can be achieved by treating mechanically exfoliated few-layer MoS_2 with a remote N_2 plasma situated 30 cm from the sample (Fig. 7(a)). N substitution on chalcogen sites was evidenced by the emergence of the N–Mo peak in XPS. It is noteworthy that N–Mo bonds showed good thermal stability and survived even after 500 °C thermal annealing in ultrahigh vacuum. This observation strongly indicates that the N atoms are chemically bonded in the lattice of MoS_2, and are not physisorbed on the surface. The N density in few-layer MoS_2 could be controlled from 1.16×10^{14} to 1.25×10^{15} atoms/cm^2 by increasing the N_2 plasma exposure time from 2 to 60 min. The threshold voltage of the transfer curve of the MoS_2 FETs showed a positive shift of around 20 V after N_2 plasma treatment, suggesting the expected p-type doping effect of N, although the device remained still dominantly n-type (Fig. 7(b)). The hole density of N-doped MoS_2 was estimated to range from 2.5×10^{18} to 1.5×10^{19} cm^{-3}, higher than that of undoped MoS_2 (~ 1.5×10^{18} cm^{-3}). The same research group also reported that N-doping can be achieved in few-layer WSe_2 by similar N_2 plasma treatment [119]. Yang et al. [115] reported synthesis of N-doped MoS_2 by 900 °C thermal annealing of commercial MoS_2 under NH_3 atmosphere, and showed its enhanced hydrogen evolution reaction activity compared to undoped MoS_2.

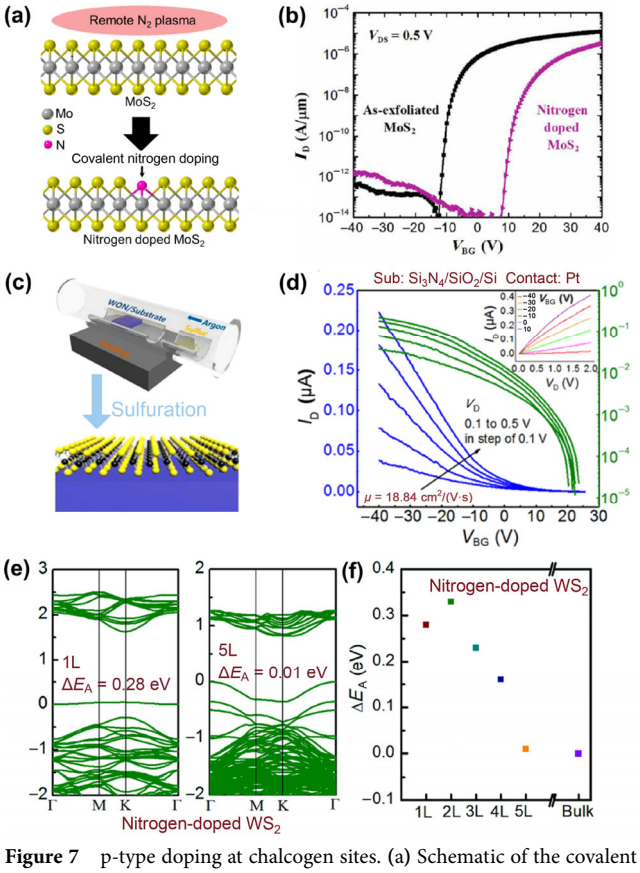

Figure 7 p-type doping at chalcogen sites. (a) Schematic of the covalent nitrogen doping of MoS_2 using remote N_2 plasma treatment. (b) Transfer characteristics of as-exfoliated (black) and N-doped (purple) few-layer MoS_2 FETs. (c) Schematic illustrating the synthesis of N:WS_2 by sulfurization of WO_xN_y film. (d) Transfer characteristics of N-doped WS_2 FETs with Pt contact on a $Si_3N_4/SiO_2/Si$ substrate. (e) Band structure of monolayer and five-layer N-doped WS_2. (f) The acceptor ionization energy (ΔE_A) as a function of layer number of N-doped MoS_2. (a) and (b) are reprinted with permission from Ref. [106], © American Chemical Society 2016. (c)–(f) are reprinted with permission from Ref. [114], © American Chemical Society 2017.

Cao et al. [114] reported the growth of N-doped WS_2 by sulfurizing atomic layer deposition grown WO_xN_y films in a sulfur vapor environment at 950 °C (Fig. 7(c)). The presence of nitrogen was verified by the N1s XPS feature in the sulfurized film and its doping density was calculated to be 4.5%. Notably, N-doped few-layer WS_2 exhibited typical p-type transfer curves (Fig. 7(d)), in contrast to N-doped few-layer MoS_2, which remained predominantly n-type. The optimized N-doped WS_2 device with Pt contacts demonstrated a room temperature field-effect hole mobility of 18.8 $cm^2/(V·s)$. This mobility is of the same order of magnitude as the electron mobility of the undoped material [114], suggesting limited detrimental impact on carrier transport even in the high impurity density regime. DFT calculations showed that the ionization energy of N-derived acceptor states is 0.28 and 0.01 eV for monolayer and five-layer WS_2 (Figs. 7(e) and 7(f)). Thus, for sufficiently thick WS_2, N acts as a good p-type dopant at room temperature.

P is an alternative p-type dopant for TMDs. Due to the widespread use of P doping in Si manufacturing, P doping is a mature technology. Plasma immersion ion implantation (PIII) is a complementary-metal-oxide-semiconductor (CMOS) compatible technology which uses a PH_3 gas source to introduce P in Si. Nipane et al. [107] demonstrated both degenerate and non-degenerate p-type doping in exfoliated few-layer MoS_2 using the PIII method with a PH_3 gas source. Field-effect hole mobilities of 8.4 and 137.7 $cm^2/(V·s)$, and hole densities of 2.4×10^{12} and 1.3×10^{10} cm^{-2}, were achieved in the degenerately and non-degenerately doped FET devices, respectively. Using area-selective P doping in exfoliated few-layer MoS_2, Nipane et al. [107] further fabricated lateral p-n homojunctions. The p-n homojunctions exhibited gate-tunable rectification ratios up to 2×10^4 and considerable stability at 300 °C and after 7 days aging. XPS characterizations and DFT simulations showed that p-type doping primarily results from both the substitution and surface adsorption of P. However, plasma immersion has the detrimental effects of etching the top few layers of TMDs in the reactive plasma. Thus, minimizing this etching effect is key to making this technology practical for 2D TMDs. It is worth noting that unlike the case for metal site doping, the bonding configuration of group 15 and 17 dopants still remains elusive. Thus, direct, atomically-resolved microscopic characterization is needed for the detailed analysis of their bonding state.

4.3 Isoelectronic doping

There are two types of substitution geometries for the chalcogen site isoelectronic doping: single site substitution and double site substitution. This means that the group 16 elements (O, S, Se or Te) randomly replace either one or two chalcogen atoms in the unit cell of the host MX_2 lattice, forming a ternary alloy $MX_{2-n}Z_n$. Due to the similar electronegativity of S, Se, and Te, and similar trigonal prismatic geometries of TMDs, the band structure of $MX_{2-n}Z_n$ alloy is similar to that of its constituents, MX_2 and MZ_2. The exception is alloying with MO_2, where the metal coordination can be locally octahedral. The bandgap of $MX_{2-n}Z_n$ can be continuously tuned from the bandgap of MX_2 to that of MZ_2 by increasing n from 0 to 2, making it possible to continuously modify the electronic and optical properties of these materials [101].

Significant efforts have been devoted to the synthesis of 2D monolayer $MS_{2-n}Se_n$ alloys by direct growth and post-growth treatments. CVD-growth of monolayer $MoS_{2-n}Se_n$ alloys was first reported in 2014 [110]. Both single- and double-Se substitution sites were found to be randomly and uniformly distributed in the host lattice for a 12% Se-doped MoS_2 monolayer (Fig. 8(a)).

CVD-growth of monolayer $MoS_{2-n}Se_n$ and $WS_{2-n}Se_n$ alloys with a series of doping or alloying densities was subsequently reported [110, 120, 121]. PL characterization showed that all the monolayer $MoS_{2-n}Se_n$ and $WS_{2-n}Se_n$ alloys are direct bandgap semiconductors with a continuously tuneable optical bandgap of 1.55–1.85 and 1.6–2.0 eV, respectively (Fig. 8(b)). FETs made with $WS_{2-n}Se_n$ alloys showed a transition from n-type to p-type character when n was increased from 0 to 2 (Fig. 8(c)). The origin of this carrier doping effect is unclear and the apparent doping may be affected by extrinsic effects such as metal contacts, but the trend is consistent with the n- and p-type character of the constituents WS_2 and WSe_2. Furthermore, the bandgap tunability of $WS_{2-n}Se_n$ alloys can be exploited for versatile band alignment engineering of WS_2-$WS_{2-n}Se_n$ monolayer lateral heterojunctions. Such a heterojunction has been realized by controlling WS_2/WSe_2 ratios in physical vapour deposition (PVD) [111].

Li et al. [112] reported direct growth of Se-substituted $MoTe_2$ alloys by CVD. Pure CVD-grown $MoTe_2$ and $MoSe_2$ are in T_d and 2H structural phases with metallic and semiconducting electronic band structures, respectively. Increasing the Se content in $MoTe_2$ resulted in T_d–1T'–2H phase transitions. Interestingly, the superconducting transition temperature of $MoTe_2$ is found to increase from 0.1 to 3.6 K with increasing Se content as the structural phase changed from T_d to 1T'. A superconductor-to-insulator transition was observed by further increasing the Se content above a critical value. This tunability makes these alloys attractive for the study of disorder-driven quantum phase transitions [122].

Despite the isovalency, oxygen doping of TMDs is distinct from other chalcogen isoelectronic doping in that oxygen is strongly electronegative and MO_2 compounds are structurally and electronically different from group 6 TMDs. Nevertheless, at low concentrations, it is possible to introduce O at the chalcogen sites in monolayer TMDs without disrupting the hexagonal lattice [113, 123–125]. It is important to understand the role of oxygen substitutional doping because TMD monolayers are prone to spontaneous oxidation in ambient conditions, especially in the presence of pre-existing defects such as grain boundaries [113, 123]. Pető et al. [113] systematically investigated the basal plane oxygen substitution of freshly exfoliated monolayer MoS_2 on Au (111) using the scanning tunnelling microscopy (STM). They found that the basal plane of MoS_2 was oxidized at room temperature under ambient condition with a slow reaction rate of 1 atom/(min·μm^2). After a month of ambient exposure, the oxygen substitution density increased from 10^{11}–10^{12} to 3×10^{12}–2×10^{13} cm^{-2} (Fig. 8(d)). Oxygen substitution is expected to play an important role in passivating the mid-gap states introduced by S vacancies in MoS_2 (Fig. 8(e)) [113]. Barja et al. [123] identified oxygen substitution in molecular beam epitaxy (MBE)-grown monolayer $MoSe_2$ and CVD-grown monolayer WS_2 using STM, and investigated its effect on their bandgap with STS. There were no noticeable deep mid-gap states at substitutional oxygen sites for both $MoSe_2$ and WS_2 (Figs. 8(f) and 8(g)), supporting the theoretical predictions on the vacancy passivation effect of oxygen substitution in the basal plane of TMDs [124–127]. It has also been suggested that basal plane oxygen substitution density exceeding 28% leads to formation of mid-gap states in MoS_2 [127]. In contrast, oxygen termination of zigzag metal edges of WS_2, which are metallic in character [128] results in small gap opening [129].

Oxygen plasma treatment is another approach for incorporating oxygen in a TMD lattice [130–132]. However, the observed carrier doping effects are so far inconsistent [130, 132].

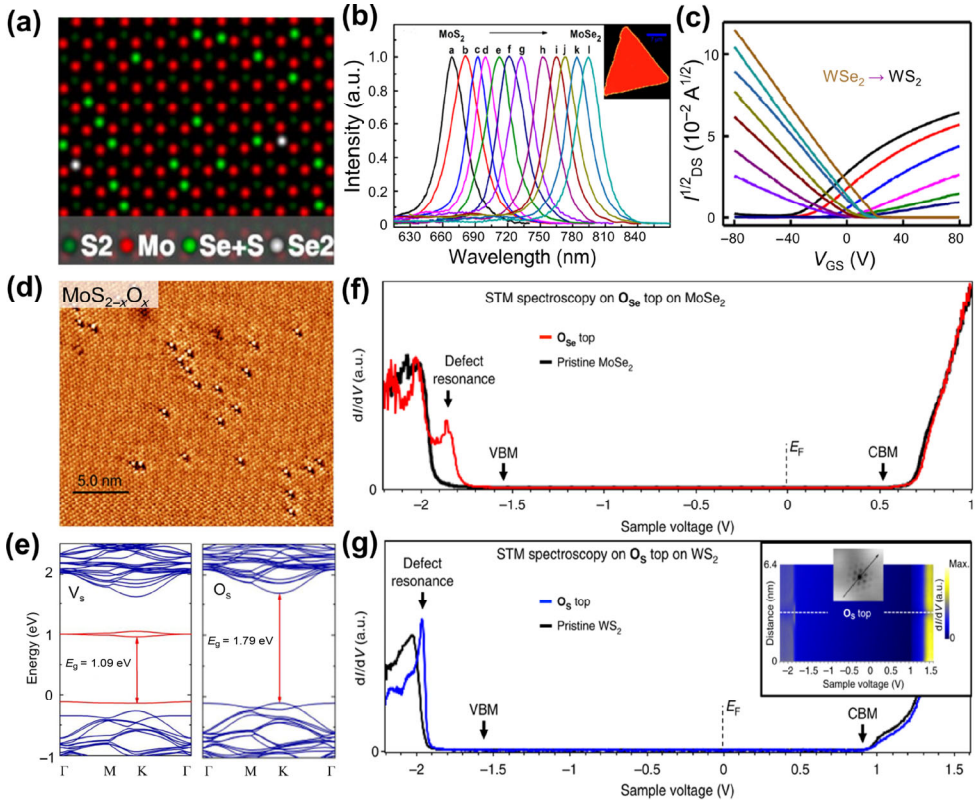

Figure 8 Isoelectronic doping at chalcogen sites. (a) Atomic structure of Se-substituted single-layer MoS_2 obtained from histogram analysis of the STEM image showing both the single- and double-Se substitution. The local Se density is ~ 12%. (b) Normalized PL spectra of monolayer $MoS_{2-n}Se_n$ (n = 0 to 2 from left to right). Inset: a typical PL mapping of a single ternary nanosheet (scale bar, 7 μm). (c) Transfer characteristics ($I_{DS}^{1/2}$–V_{GS} plot) of monolayer WSe_2S_{2-n} FET from nearly pure WSe_2 (brown curve) to nearly pure WS_2 (black curve). (d) Atomic-resolution STM image (5 mV, 2 nA) of an exfoliated MoS_2 single-layer after 1 month of ambient exposure. (e) DFT band structure of MoS_2 with isolated sulfur vacancies (left) and with oxygen substitution on the S sites (right). (f) Representative STS spectrum (dI/dV) of substitutional oxygen O_{Se} (red line), and of a pristine region of monolayer $MoSe_2$ (black line) grown by MBE. (g) Representative STS spectra of substitutional oxygen O_S (blue line), and of a pristine region of monolayer WS_2 (black line) grown by chemical vapor deposition. Inset: spatially resolved dI/dV conductance scan across a single O_S defect. (a) is reprinted with permission from Ref. [110], © American Chemical Society 2014. (b) is reprinted with permission from Ref. [120], © American Chemical Society 2014. (c) is reprinted with permission from Ref. [121], © American Chemical Society 2016. (d) and (e) are reprinted with permission from Ref. [113], © Springer Nature 2018. (f) and (g) are reprinted with permission from Ref. [123], © Barja, S. et al. 2019.

This may be due to unintentional etching and uncontrolled surface adsorption effects. Substitutional doping by oxygen plasma treatment is yet to be verified.

5 Conclusion and outlook

Substitutional doping of 2D group 6 TMDs is a promising route to unlocking the full potential of these emerging materials for device applications. The wide variety of chemical elements that can be readily incorporated into the lattice of TMDs highlights the versatility of this system and presents vast opportunities for electronic structure engineering and fundamental studies (Table 2). The current research, however, is still at an early stage and a number of open questions remain. In terms of doping techniques, a precise control of doping densities, especially in the low-density limits (< 10^{10} cm^{-2}), is an immediate goal. The widely-used powder CVD method is highly versatile for bottom-up growth of doped materials, but its controllability and scalability are limited for practical use. In this respect, MOCVD [67] has shown promising results albeit for a limited number of dopants. For chalcogen site substitution, post-growth treatment is promising but density control is still a challenge. Successful development of a precise doping technique is contingent on the ability to identify and quantify impurities. Due to the atomically-thin body of the material, impurity atoms in ppm concentrations cannot be detected by common techniques such as XPS. Advanced techniques such as atomic resolution, aberration-corrected STEM imaging and electron energy loss spectroscopy may become essential for identifying individual impurity species, their bonding configuration, and the local strain environment in the host material [133–135]. High spatial resolution characterization techniques such as nano-angle-resolved photoemission spectroscopy [136], STS [137], and nano-optical [138–141] techniques are also crucial for investigating the local electronic structure around individual dopant impurities.

Studies to date showed that the impact of doping on the electrical properties of 2D TMDs is often unpredictable. For example, Mn, which is expected to be an n-type dopant, has so far shown contradicting results with no clear sign of carrier density enhancement [69–71]. The complexity of the problem is multifold. The large ionization energy of impurities in a 2D host often limits carrier doping. High impurity density leads to competing effects of hopping conduction [67] and scattering-limited band transport [41, 71, 86]. There are also indirect effects such as changes in intrinsic defect density and types. Since the physical properties of TMDs are strongly influenced by chalcogen vacancies that are present in high concentrations (10^{13} to 10^{14} cm^{-2}) [142, 143], intentionally introduced impurities may indirectly modulate the carrier density of the host material by altering the stability of such vacancy defects [66, 93]. Nevertheless, systems such as V-doped WSe_2 and V-doped WS_2 have so far shown a clear sign of expected hole doping, indicating sufficiently small impurity ionization energy [44, 86],

Table 2 Summary of experimental reports on substitutionally doped 2D group 6 TMDs[a]

Doping sites	Dopants	Host	Observed doping	Doping density (%)	Doping method	References
M-dopant	Re	MoS_2	n	1	CVD with solid oxide	[66]
		MoS_2	n	0.3	CVD with solid oxide	[23]
		MoS_2	n	0.3	CVD with liquid precursor	[24]
		MoS_2	—	9	MOCVD	[67]
		WS_2	n	10	CVD with molten oxide	[154]
	Mn	MoS_2	n	2	CVD with solid oxide	[69]
		MoS_2	n	1.80	CVD with molten oxide	[70]
		MoS_2	p	—	CVD with metal	[71]
	Fe	MoS_2	n	0.53	CVT	[41]
		MoS_2	—	0.3–0.5	CVD with solid oxide	[44]
		MoS_2	—	2	CVD with metal and metal sulfide	[73]
	Co	MoS_2	n	16.00	CVD with solid oxide	[76]
		MoS_2	p	1	CVD with solid precursor	[34]
	Cu	MoS_2	n	11.76	CVT	[75]
	Nb	MoS_2	p	4–19	MOCVD	[67]
		MoS_2	p	0.5	CVT	[82]
		MoS_2	p	0.8	CVD with molten oxide	[79]
		WS_2	p	1.40	CVD with molten oxide	[80]
		WS_2	p	6.70	CVD with solid oxide	[23]
		WSe_2	p	1.50	CVD with solid oxide	[155]
		WSe_2	p	2–29	CVD with liquid precursor	[83]
	V	WSe_2	p	0.1–10	CVD with liquid precursor	[86]
		WS_2	p	0.4, 2, 8	CVD with liquid precursor	[85]
		WSe_2	—	3	MBE	[87]
	Zn	MoS_2	p	1–2	CVD with solid oxide	[39]
	Sb	MoS_2	—	9	CVD with solid oxide	[42]
	W	$MoSe_2$	p	2, 7, 18	CVD with solid oxide	[93, 95]
	Mo	WS_2	—	—	CVD with solid oxide	[100]
	Cr	MoS_2	n	—	CVD with metal	[71]
X-dopant	Cl	MoS_2, WS_2	n	—	DCE soaking	[108]
		MoS_2	n	—	CVD with $HAuCl_4$	[109]
	N	MoS_2	p	1–8	N_2 Plasma treatment	[106]
		WSe_2	p	—	N_2 Plasma treatment	[119]
		WS_2	p	4.5	Sulfurization of WO_xN_y film	[109]
		MoS_2	—	0.2–0.6	NH_3 annealing	[115]
	P	MoS_2	p	—	PH_3 plasma treatment	[107]
	Se	MoS_2	—	0–100	CVD with solid oxide	[110, 120]
		WS_2	p	0–100	PVD	[111, 121]
		$MoTe_2$	—	0–65	CVD with solid oxide	[112]
	O	MoS_2, WS_2	—	—	Spontaneous oxidation	[123]
		MoS_2, $MoSe_2$	—	0.3–8.7	Spontaneous oxidation	[113]
		MoS_2	p	13	O_2 plasma treatment	[130]
		MoS_2	n	15.6	O_2 plasma treatment	[132]
		MoS_2	—	—	O_2 plasma treatment	[131]

[a]CVD with solid oxide: metal oxides are used precursors; CVD with liquid precursor: water dissolvable metal compounds are used as precursors; CVD with molten oxide: mixtures of salt and metal oxide are used as precursors.

unlike the case of Nb-doped MoS_2 monolayer where p-type conduction enhancement is often marginal [79], unless an alloying impurity density is reached [67]. Identifying the suitable elements for versatile carrier modulation for different host material remains a crucial task.

Substitutional doping is not only important for carrier modulation but for a variety of novel functionalities. While the large ionization energy of impurities is detrimental for carrier doping, it can be advantageous for quantum photonics applications. Impurity bound excitons are known to serve as single photon light sources in conventional quantum wells such as N-doped ZnSe [144]. Bound exciton complexes in TMDs are expected to be strongly bound to impurities and offer opportunities for quantum photonic applications [145, 146].

Defect complexes such as $Re_{Mo}V_S$ in Re:MoS_2 are also predicted to act as a two-level quantum system, allowing single photon emission [147]. Furthermore, magnetically doped 2D TMDs have become a fertile ground for fundamental discoveries in recent years [44, 68, 86, 148, 149] and hold promise for spintronics [38, 72, 150–153]. A continued collective effort to develop doping techniques and access impurity-induced physical phenomena is therefore key to enabling novel technologies based on 2D materials.

Acknowledgements

The authors acknowledge support from the Ministry of Education (MOE), Singapore, under AcRF Tier 3 (MOE2018-T3-1-005) and the Singapore National Research Foundation for funding the research under medium-sized centre programme. M. B. acknowledges support from MOE's AcRF Tier 1 (R-284-000-179-133).

References

[1] Avouris, P.; Heinz, T. F.; Low, T. *2D Materials*; Cambridge University Press: Cambridge, 2017.

[2] Novoselov, K. S.; Mishchenko, A.; Carvalho, A.; Castro Neto, A. H. 2D materials and van der Waals heterostructures. *Science* **2016**, *353*, aac9439.

[3] Manzeli, S.; Ovchinnikov, D.; Pasquier, D.; Yazyev, O. V.; Kis, A. 2D transition metal dichalcogenides. *Nat. Rev. Mater.* **2017**, *2*, 17033.

[4] Splendiani, A.; Sun, L.; Zhang, Y. B.; Li, T. S.; Kim, J.; Chim, C. Y.; Galli, G.; Wang, F. Emerging photoluminescence in monolayer MoS_2. *Nano Lett.* **2010**, *10*, 1271–1275.

[5] Mak, K. F.; Lee, C.; Hone, J.; Shan, J.; Heinz, T. F. Atomically thin MoS_2: A new direct-gap semiconductor. *Phys. Rev. Lett.* **2010**, *105*, 136805.

[6] Radisavljevic, B.; Radenovic, A.; Brivio, J.; Giacometti, V.; Kis, A. Single-layer MoS_2 transistors. *Nat. Nanotechnol.* **2011**, *6*, 147–150.

[7] Schmidt, H.; Giustiniano, F.; Eda, G. Electronic transport properties of transition metal dichalcogenide field-effect devices: Surface and interface effects. *Chem. Soc. Rev.* **2015**, *44*, 7715–7736.

[8] Yoon, Y.; Ganapathi, K.; Salahuddin, S. How good can monolayer MoS_2 transistors be? *Nano Lett.* **2011**, *11*, 3768–3773.

[9] Chhowalla, M.; Jena, D.; Zhang, H. Two-dimensional semiconductors for transistors. *Nat. Rev. Mater.* **2016**, *1*, 16052.

[10] Desai, S. B.; Madhvapathy, S. R.; Sachid, A. B.; Llinas, J. P.; Wang, Q. X.; Ahn, G. H.; Pitner, G.; Kim, M. J.; Bokor, J.; Hu, C. M. et al. MoS_2 transistors with 1-nanometer gate lengths. *Science* **2016**, *354*, 99–102.

[11] Vu, Q. A.; Shin, Y. S.; Kim, Y. R.; Nguyen, V. L.; Kang, W. T.; Kim, H.; Luong, D. H.; Lee, I. M.; Lee, K.; Ko, D. S. et al. Two-terminal floating-gate memory with van der Waals heterostructures for ultrahigh on/off ratio. *Nat. Commun.* **2016**, *7*, 12725.

[12] Radisavljevic, B.; Whitwick, M. B.; Kis, A. Integrated circuits and logic operations based on single-layer MoS_2. *ACS Nano* **2011**, *5*, 9934–9938.

[13] Koppens, F. H. L.; Mueller, T.; Avouris, P.; Ferrari, A. C.; Vitiello, M. S.; Polini, M. Photodetectors based on graphene, other two-dimensional materials and hybrid systems. *Nat. Nanotechnol.* **2014**, *9*, 780–793.

[14] Lopez-Sanchez, O.; Lembke, D.; Kayci, M.; Radenovic, A.; Kis, A. Ultrasensitive photodetectors based on monolayer MoS_2. *Nat. Nanotechnol.* **2013**, *8*, 497–501.

[15] Konstantatos, G. Current status and technological prospect of photodetectors based on two-dimensional materials. *Nat. Commun.* **2018**, *9*, 5266.

[16] Ross, J. S.; Klement, P.; Jones, A. M.; Ghimire, N. J.; Yan, J. Q.; Mandrus, D. G.; Taniguchi, T.; Watanabe, K.; Kitamura, K.; Yao, W. et al. Electrically tunable excitonic light-emitting diodes based on monolayer WSe_2 p–n junctions. *Nat. Nanotechnol.* **2014**, *9*, 268–272.

[17] Sundaram, R. S.; Engel, M.; Lombardo, A.; Krupke, R.; Ferrari, A. C.; Avouris, P.; Steiner, M. Electroluminescence in single layer MoS_2. *Nano Lett.* **2013**, *13*, 1416–1421.

[18] Wang, J. Y.; Verzhbitskiy, I.; Eda, G. Electroluminescent devices based on 2D semiconducting transition metal dichalcogenides. *Adv. Mater.* **2018**, *30*, 1802687.

[19] Datta, I.; Chae, S. H.; Bhatt, G. R.; Tadayon, M. A.; Li, B. C.; Yu, Y. L.; Park, C.; Park, J.; Cao, L. Y.; Basov, D. N. et al. Low-loss composite photonic platform based on 2D semiconductor monolayers. *Nat. Photonics* **2020**, *14*, 256–262.

[20] Lee, H. S.; Min, S. W.; Chang, Y. G.; Park, M. K.; Nam, T.; Kim, H.; Kim, J. H.; Ryu, S.; Im, S. MoS_2 nanosheet phototransistors with thickness-modulated optical energy gap. *Nano Lett.* **2012**, *12*, 3695–3700.

[21] Sun, Z. P.; Martinez, A.; Wang, F. Optical modulators with 2D layered materials. *Nat. Photonics* **2016**, *10*, 227–238.

[22] Zhou, J. D.; Lin, J. H.; Huang, X. W.; Zhou, Y.; Chen, Y.; Xia, J.; Wang, H.; Xie, Y.; Yu, H. M.; Lei, J. C. et al. A library of atomically thin metal chalcogenides. *Nature* **2018**, *556*, 355–359.

[23] Gao, J.; Kim, Y. D.; Liang, L. B.; Idrobo, J. C.; Chow, P.; Tan, J. W.; Li, B. C.; Li, L.; Sumpter, B. G.; Lu, T. M. et al. Transition-metal substitution doping in synthetic atomically thin semiconductors. *Adv. Mater.* **2016**, *28*, 9735–9743.

[24] Zhang, T. Y.; Fujisawa, K.; Zhang, F.; Liu, M. Z.; Lucking, M. C.; Gontijo, R. N.; Lei, Y.; Liu, H.; Crust, K.; Granzier-Nakajima, T. et al. Universal *in situ* substitutional doping of transition metal dichalcogenides by liquid-phase precursor-assisted synthesis. *ACS Nano* **2020**, *14*, 4326–4335.

[25] Tongay, S.; Zhou, J.; Ataca, C.; Liu, J.; Kang, J. S.; Matthews, T. S.; You, L.; Li, J. B.; Grossman, J. C.; Wu, J. Q. Broad-range modulation of light emission in two-dimensional semiconductors by molecular physisorption gating. *Nano Lett.* **2013**, *13*, 2831–2836.

[26] Mouri, S.; Miyauchi, Y.; Matsuda, K. Tunable photoluminescence of monolayer MoS_2 via chemical doping. *Nano Lett.* **2013**, *13*, 5944–5948.

[27] Kiriya, D.; Tosun, M.; Zhao, P. D.; Kang, J. S.; Javey, A. Air-stable surface charge transfer doping of MoS_2 by benzyl viologen. *J. Am. Chem. Soc.* **2014**, *136*, 7853–7856.

[28] Jung, Y.; Zhou, Y.; Cha, J. J. Intercalation in two-dimensional transition metal chalcogenides. *Inorg. Chem. Front.* **2016**, *3*, 452–463.

[29] Chanana, A.; Mahapatra, S. Theoretical insights to niobium-doped monolayer MoS_2–gold contact. *IEEE Trans. Electron Dev.* **2015**, *62*, 2346–2351.

[30] Lin, X. Q.; Ni, J. Charge and magnetic states of Mn-, Fe-, and Co-doped monolayer MoS_2. *J. Appl. Phys.* **2014**, *116*, 044311.

[31] Luo, M.; Shen, Y. H.; Chu, J. H. First-principles study of the magnetism of Ni-doped MoS_2 monolayer. *Jpn. J. Appl. Phys.* **2016**, *55*, 093001.

[32] Dolui, K.; Rungger, I.; Pemmaraju, C. D.; Sanvito, S. Possible doping strategies for MoS_2 monolayers: An *ab initio* study. *Phys. Rev. B* **2013**, *88*, 075420.

[33] Zhao, X.; Chen, P.; Xia, C. X.; Wang, T. X.; Dai, X. Q. Electronic and magnetic properties of n-type and p-doped MoS_2 monolayers. *RSC Adv.* **2016**, *6*, 16772–16778.

[34] Fan, X. L.; An, Y. R.; Guo, W. J. Ferromagnetism in transitional metal-doped MoS_2 monolayer. *Nanoscale Res. Lett.* **2016**, *11*, 154.

[35] Williamson, I.; Li, S. S.; Correa Hernandez, A.; Lawson, M.; Chen, Y.; Li, L. Structural, electrical, phonon, and optical properties of Ti- and V-doped two-dimensional MoS_2. *Chem. Phys. Lett.* **2017**, *674*, 157–163.

[36] Zhao, X.; Xia, C. X.; Wang, T. X.; Dai, X. Q. Electronic and magnetic properties of X-doped (X = Ti, Zr, Hf) tungsten disulphide monolayer. *J. Alloys Compd.* **2016**, *654*, 574–579.

[37] Carvalho, A.; Neto, A. H. C. Donor and acceptor levels in semiconducting transition-metal dichalcogenides. *Phys. Rev. B* **2014**, *89*, 081406.

[38] Duan, H. L.; Guo, P.; Wang, C.; Tan, H.; Hu, W.; Yan, W. S.; Ma, C.; Cai, L.; Song, L.; Zhang, W. H. et al. Beating the exclusion rule against the coexistence of robust luminescence and ferromagnetism in chalcogenide monolayers. *Nat. Commun.* **2019**, *10*, 1584.

[39] Xu, E. Z.; Liu, H. M.; Park, K.; Li, Z.; Losovyj, Y.; Starr, M.; Werbianskyj, M.; Fertig, H. A.; Zhang, S. X. P-type transition-metal doping of large-area MoS_2 thin films grown by chemical vapor deposition. *Nanoscale* **2017**, *9*, 3576–3584.
[40] Lin, Y. C.; Dumcenco, D. O.; Komsa, H. P.; Niimi, Y.; Krasheninnikov, A. V.; Huang, Y. S.; Suenaga, K. Properties of individual dopant atoms in single-layer MoS_2: Atomic structure, migration, and enhanced reactivity. *Adv. Mater.* **2014**, *26*, 2857–2861.
[41] Wang, S. Y.; Ko, T. S.; Huang, C. C.; Lin, D. Y.; Huang, Y. S. Optical and electrical properties of MoS_2 and Fe-doped MoS_2. *Jpn. J. Appl. Phys.* **2014**, *53*, 04EH07.
[42] Zhong, M. Z.; Shen, C.; Huang, L.; Deng, H. X.; Shen, G. Z.; Zheng, H. Z.; Wei, Z. M.; Li, J. B. Electronic structure and exciton shifts in Sb-doped MoS_2 monolayer. *npj 2D Mater. Appl.* **2019**, *3*, 1.
[43] Xiang, Z. C.; Zhang, Z.; Xu, X. J.; Zhang, Q.; Wang, Q. B.; Yuan, C. W. Room-temperature ferromagnetism in Co doped MoS_2 sheets. *Phys. Chem. Chem. Phys.* **2015**, *17*, 15822–15828.
[44] Fu, S. C.; Kang, K.; Shayan, K.; Yoshimura, A.; Dadras, S.; Wang, X. T.; Zhang, L. H.; Chen, S. W.; Liu, N.; Jindal, A. et al. Enabling room temperature ferromagnetism in monolayer MoS_2 via *in situ* iron-doping. *Nat. Commun.* **2020**, *11*, 2034.
[45] Habib, M.; Muhammad, Z.; Khan, R.; Wu, C. Q.; ur Rehman, Z.; Zhou, Y.; Liu, H. J.; Song, L. Ferromagnetism in CVT grown tungsten diselenide single crystals with nickel doping. *Nanotechnology* **2018**, *29*, 115701.
[46] Wilson, J.; Yoffe, A. D. The transition metal dichalcogenides discussion and interpretation of the observed optical, electrical and structural properties. *Adv. Phys.* **1969**, *18*, 193–335.
[47] Brixner, L. H. Preparation and properties of the single crystalline AB_2-type selenides and tellurides of niobium, tantalum, molybdenum and tungsten. *J. Inorg. Nucl. Chem.* **1962**, *24*, 257–263.
[48] Hicks, W. Semiconducting behavior of substituted tungsten diselenide and its analogues. *J. Electrochem. Soc.* **1964**, *111*, 1058–1065.
[49] Luo, P.; Zhuge, F. W.; Zhang, Q. F.; Chen, Y. Q.; Lv, L.; Huang, Y.; Li, H. Q.; Zhai, T. Y. Doping engineering and functionalization of two-dimensional metal chalcogenides. *Nanoscale Horiz.* **2019**, *4*, 26–51.
[50] Zhang, K. H.; Robinson, J. Doping of two-dimensional semiconductors: A rapid review and outlook. *MRS Adv.* **2019**, *4*, 2743–2757.
[51] Yoon, A.; Lee, Z. Synthesis and properties of two dimensional doped transition metal dichalcogenides. *Appl. Microsc.* **2017**, *47*, 19–28.
[52] Cheiwchanchamnangij, T.; Lambrecht, W. R. L. Quasiparticle band structure calculation of monolayer, bilayer, and bulk MoS_2. *Phys. Rev. B* **2012**, *85*, 205302.
[53] Molina-Sánchez, A.; Wirtz, L. Phonons in single-layer and few-layer MoS_2 and WS_2. *Phys. Rev. B* **2011**, *84*, 155413.
[54] Reshak, A. H.; Auluck, S. Calculated optical properties of 2H-MoS_2 intercalated with lithium. *Phys. Rev. B* **2003**, *68*, 125101.
[55] Chen, X. L.; Wu, Z. F.; Xu, S. G.; Wang, L.; Huang, R.; Han, Y.; Ye, W. G.; Xiong, W.; Han, T. Y.; Long, G. et al. Probing the electron states and metal-insulator transition mechanisms in molybdenum disulphide vertical heterostructures. *Nat. Commun.* **2015**, *6*, 6088.
[56] Komsa, H. P.; Krasheninnikov, A. V. Effects of confinement and environment on the electronic structure and exciton binding energy of MoS_2 from first principles. *Phys. Rev. B* **2012**, *86*, 241201.
[57] Chernikov, A.; Berkelbach, T. C.; Hill, H. M.; Rigosi, A.; Li, Y. L.; Aslan, O. B.; Reichman, D. R.; Hybertsen, M. S.; Heinz, T. F. Exciton binding energy and nonhydrogenic Rydberg series in monolayer WS_2. *Phys. Rev. Lett.* **2014**, *113*, 076802.
[58] Ugeda, M. M.; Bradley, A. J.; Shi, S. F.; da Jornada, F. H.; Zhang, Y.; Qiu, D. Y.; Ruan, W.; Mo, S. K.; Hussain, Z.; Shen, Z. X. et al. Giant bandgap renormalization and excitonic effects in a monolayer transition metal dichalcogenide semiconductor. *Nat. Mater.* **2014**, *13*, 1091–1095.
[59] Li, J. B.; Wei, S. H.; Wang, L. W. Stability of the DX^- center in GaAs quantum dots. *Phys. Rev. Lett.* **2005**, *94*, 185501.
[60] Yang, J. H.; Yakobson, B. I. Dimensionality-suppressed chemical doping in 2D semiconductors: The cases of phosphorene, MoS_2, and ReS_2 from first-principles. 2017, arXiv:1711.05094. arXiv.org e-Print archive. https://arxiv.org/abs/1711.05094 (accessed Nov 14, 2017).
[61] Götz, W.; Johnson, N. M.; Chen, C.; Liu, H.; Kuo, C.; Imler, W. Activation energies of Si donors in GaN. *Appl. Phys. Lett.* **1996**, *68*, 3144–3146.
[62] Rockett, A.; Johnson, D. D.; Khare, S. V.; Tuttle, B. R. Prediction of dopant ionization energies in silicon: The importance of strain. *Phys. Rev. B* **2003**, *68*, 233208.
[63] Lu, S.; Li, C.; Zhao, Y. F.; Gong, Y. Y.; Niu, L. Y.; Liu, X. J. Tunable redox potential of nonmetal doped monolayer MoS_2: First principle calculations. *Appl. Surf. Sci.* **2016**, *384*, 360–367.
[64] Hu, A. M.; Wang, L. L.; Meng, B.; Xiao, W. Z. *Ab initio* study of magnetism in nonmagnetic metal substituted monolayer MoS_2. *Solid State Commun.* **2015**, *220*, 67–71.
[65] Noh, J. Y.; Kim, H.; Park, M.; Kim, Y. S. Deep-to-shallow level transition of Re and Nb dopants in monolayer MoS_2 with dielectric environments. *Phys. Rev. B* **2015**, *92*, 115431.
[66] Zhang, K. H.; Bersch, B. M.; Joshi, J.; Addou, R.; Cormier, C. R.; Zhang, C. X.; Xu, K.; Briggs, N. C.; Wang, K.; Subramanian, S. et al. Tuning the electronic and photonic properties of monolayer MoS_2 via *in situ* rhenium substitutional doping. *Adv. Funct. Mater.* **2018**, *28*, 1706950.
[67] Gao, H.; Suh, J.; Cao, M. C.; Joe, A. Y.; Mujid, F.; Lee, K. H.; Xie, S. E.; Poddar, P.; Lee, J. U.; Kang, K. et al. Tuning electrical conductance of MoS_2 monolayers through substitutional doping. *Nano Lett.* **2020**, *20*, 4095–4101.
[68] Kochat, V.; Apte, A.; Hachtel, J. A.; Kumazoe, H.; Krishnamoorthy, A.; Susarla, S.; Idrobo, J. C.; Shimojo, F.; Vashishta, P.; Kalia, R. et al. Re doping in 2D transition metal dichalcogenides as a new route to tailor structural phases and induced magnetism. *Adv. Mater.* **2017**, *29*, 1703754.
[69] Zhang, K. H.; Feng, S. M.; Wang, J. J.; Azcatl, A.; Lu, N.; Addou, R.; Wang, N.; Zhou, C. J.; Lerach, J.; Bojan, V. et al. Manganese doping of monolayer MoS_2: The substrate is critical. *Nano Lett.* **2015**, *15*, 6586–6591.
[70] Cai, Z. Y.; Shen, T. Z.; Zhu, Q.; Feng, S. M.; Yu, Q. M.; Liu, J. M.; Tang, L.; Zhao, Y.; Wang, J. W.; Liu, B. L. et al. Dual-additive assisted chemical vapor deposition for the growth of Mn-doped 2D MoS_2 with tunable electronic properties. *Small* **2020**, *16*, 1903181.
[71] Huang, C.; Jin, Y. B.; Wang, W. Y.; Tang, L.; Song, C. Y.; Xiu, F. X. Manganese and chromium doping in atomically thin MoS_2. *J. Semicond.* **2017**, *38*, 033004.
[72] Cheng, Y. C.; Zhu, Z. Y.; Mi, W. B.; Guo, Z. B.; Schwingenschlögl, U. Prediction of two-dimensional diluted magnetic semiconductors: Doped monolayer MoS_2 systems. *Phys. Rev. B* **2013**, *87*, 100401.
[73] Li, Q.; Zhao, X. X.; Deng, L. J.; Shi, Z. T.; Liu, S.; Wei, Q. L.; Zhang, L. B.; Cheng, Y. C.; Zhang, L.; Lu, H. P. et al. Enhanced valley Zeeman splitting in Fe-doped monolayer MoS_2. *ACS Nano* **2020**, *14*, 4636–4645.
[74] Lu, S. C.; Leburton, J. P. Electronic structures of defects and magnetic impurities in MoS_2 monolayers. *Nanoscale Res. Lett.* **2014**, *9*, 676.
[75] Liu, M. M.; Wei, S. C.; Shahi, S.; Jaiswal, H. N.; Paletti, P.; Fathipour, S.; Remskar, M.; Jiao, J.; Hwang, W.; Yao, F. et al. Enhanced carrier transport by transition metal doping in WS_2 field effect transistors. *Nanoscale*, in press, DOI: 10.1039/D0NR01573C.
[76] Li, B.; Huang, L.; Zhong, M. Z.; Huo, N. J.; Li, Y. T.; Yang, S. X.; Fan, C.; Yang, J. H.; Hu, W. P.; Wei, Z. M. et al. Synthesis and transport properties of large-scale alloy $Co_{0.16}Mo_{0.84}S_2$ bilayer nanosheets. *ACS Nano* **2015**, *9*, 1257–1262.
[77] Hu, A. M.; Wang, L. L.; Xiao, W. Z.; Meng, B. Electronic structures and magnetic properties in Cu-doped two-dimensional dichalcogenides. *Phys. E: Low-Dimens. Syst. Nanostruct.* **2015**, *73*, 69–75.
[78] Yun, W. S.; Lee, J. Unexpected strong magnetism of Cu doped single-layer MoS_2 and its origin. *Phys. Chem. Chem. Phys.* **2014**, *16*, 8990–8996.
[79] Li, M. G.; Yao, J. D.; Wu, X. X.; Zhang, S. C.; Xing, B. R.; Niu, X. Y.; Yan, X. Y.; Yu, Y.; Liu, Y. L.; Wang, Y. W. P-type doping in large-area monolayer MoS_2 by chemical vapor deposition. *ACS Appl. Mater. Interfaces* **2020**, *12*, 6276–6282.
[80] Jin, Y. Y.; Zeng, Z. Y.; Xu, Z. W.; Lin, Y. C.; Bi, K. X.; Shao, G. L.; Hu, T. S.; Wang, S. S.; Li, S. S.; Suenaga, K. et al. Synthesis and transport properties of degenerate p-type Nb-doped WS_2 monolayers. *Chem. Mater.* **2019**, *31*, 3534–3541.
[81] Sasaki, S.; Kobayashi, Y.; Liu, Z.; Suenaga, K.; Maniwa, Y.; Miyauchi, Y.; Miyata, Y. Growth and optical properties of Nb-doped

WS_2 monolayers. *Appl. Phys. Express* **2016**, *9*, 071201.
[82] Suh, J.; Park, T. E.; Lin, D. Y.; Fu, D. Y.; Park, J.; Jung, H. J.; Chen, Y. B.; Ko, C.; Jang, C.; Sun, Y. H. et al. Doping against the native propensity of MoS_2: Degenerate hole doping by cation substitution. *Nano Lett.* **2014**, *14*, 6976–6982.
[83] Qin, Z. Y.; Loh, L.; Wang, J. Y.; Xu, X. M.; Zhang, Q.; Haas, B.; Alvarez, C.; Okuno, H.; Yong, J. Z.; Schultz, T. et al. Growth of Nb-doped monolayer WS_2 by liquid-phase precursor mixing. *ACS Nano* **2019**, *13*, 10768–10775.
[84] Li, S. S.; Lin, Y. C.; Zhao, W.; Wu, J.; Wang, Z.; Hu, Z. H.; Shen, Y. D.; Tang, D. M.; Wang, J. Y.; Zhang, Q. et al. Vapour–liquid–solid growth of monolayer MoS_2 nanoribbons. *Nat. Mater.* **2018**, *17*, 535–542.
[85] Zhang, F.; Zheng, B. Y.; Sebastian, A.; Olson, H.; Liu, M. Z.; Fujisawa, K.; Pham, Y. T. H.; Jimenez, V. O.; Kalappattil, V.; Miao, L. X. et al. Monolayer vanadium-doped tungsten disulfide: A room-temperature dilute magnetic semiconductor. 2020, arXiv:2005.01965. arXiv.org e-Print archive. https://arxiv.org/abs/2005.01965 (accessed May 5, 2020).
[86] Yun, S. J.; Duong, D. L.; Ha, D. M.; Singh, K.; Phan, T. L.; Choi, W.; Kim, Y. M.; Lee, Y. H. Ferromagnetic order at room temperature in monolayer WSe_2 semiconductor via vanadium dopant. *Adv. Sci.* **2020**, *7*, 1903076.
[87] Mallet, P.; Chiapello, F.; Okuno, H.; Boukari, H.; Jamet, M.; Veuillen, J. Y. Bound hole states associated to individual vanadium atoms incorporated into monolayer WSe_2. *Phys. Rev. Lett.* **2020**, *125*, 036802.
[88] Shu, C. K.; Lee, W. H.; Pan, Y. C.; Chen, C. C.; Lin, H. C.; Ou, J.; Chen, W. H.; Chen, W. K.; Lee, M. C. Optical and electrical investigations of isoelectronic In-doped GaN films. *Solid State Commun.* **2000**, *114*, 291–293.
[89] Lee, M. K.; Chiu, T. H.; Dayem, A.; Agyekum, E. Isoelectronic doping in GaAs epilayers grown by molecular beam epitaxy. *Appl. Phys. Lett.* **1988**, *53*, 2653–2655.
[90] Walukiewicz, W. Dislocation density reduction by isoelectronic impurities in semiconductors. *Appl. Phys. Lett.* **1989**, *54*, 2009–2011.
[91] Ma, Y. Y.; Tang, B. B.; Lian, W. T.; Wu, C. Y.; Wang, X. M.; Ju, H. X.; Zhu, C. F.; Fan, F. J.; Chen, T. Efficient defect passivation of Sb_2Se_3 film by tellurium doping for high performance solar cells. *J. Mater. Chem. A* **2020**, *8*, 6510–6516.
[92] Bhattacharya, P. K.; Dhar, S.; Berger, P.; Juang, F. Y. Low defect densities in molecular beam epitaxial GaAs achieved by isoelectronic In doping. *Appl. Phys. Lett.* **1986**, *49*, 470–472.
[93] Li, X. F.; Puretzky, A. A.; Sang, X. H.; KC, S.; Tian, M. K.; Ceballos, F.; Mahjouri-Samani, M.; Wang, K.; Unocic, R. R.; Zhao, H. et al. Suppression of defects and deep levels using isoelectronic tungsten substitution in monolayer $MoSe_2$. *Adv. Funct. Mater.* **2017**, *27*, 1603850.
[94] Huang, B.; Yoon, M.; Sumpter, B. G.; Wei, S. H.; Liu, F. Alloy engineering of defect properties in semiconductors: Suppression of deep levels in transition-metal dichalcogenides. *Phys. Rev. Lett.* **2015**, *115*, 126806.
[95] Li, X. F.; Lin, M. W.; Basile, L.; Hus, S. M.; Puretzky, A. A.; Lee, J.; Kuo, Y. C.; Chang, L. Y.; Wang, K.; Idrobo, J. C. et al. Isoelectronic tungsten doping in monolayer $MoSe_2$ for carrier type modulation. *Adv. Mater.* **2016**, *28*, 8240–8247.
[96] Cai, H.; Chen, B.; Blei, M.; Chang, S. L. Y.; Wu, K. D.; Zhuang, H. L.; Tongay, S. Abnormal band bowing effects in phase instability crossover region of $GaSe_{1-x}Te_x$ nanomaterials. *Nat. Commun.* **2018**, *9*, 1927.
[97] Ma, J.; Wei, S. H. Bowing of the defect formation energy in semiconductor alloys. *Phys. Rev. B* **2013**, *87*, 241201.
[98] Wei, S. H.; Zhang, S. B.; Zunger, A. First-principles calculation of band offsets, optical bowings, and defects in CdS, CdSe, CdTe, and their alloys. *J. Appl. Phys.* **2000**, *87*, 1304–1311.
[99] Song, J. G.; Ryu, G. H.; Lee, S. J.; Sim, S.; Lee, C. W.; Choi, T.; Jung, H.; Kim, Y.; Lee, Z.; Myoung, J. M. et al. Controllable synthesis of molybdenum tungsten disulfide alloy for vertically composition-controlled multilayer. *Nat. Commun.* **2015**, *6*, 7817.
[100] Azizi, A.; Wang, Y.; Stone, G.; Elias, A. L.; Lin, Z.; Terrones, M.; Crespi, V. H.; Alem, N. Defect coupling and sub-angstrom structural distortions in $W_{1-x}Mo_xS_2$ monolayers. *Nano Lett.* **2017**, *17*, 2802–2808.
[101] Karthikeyan, J.; Komsa, H. P.; Batzill, M.; Krasheninnikov, A. V. Which transition metal atoms can be embedded into two-dimensional molybdenum dichalcogenides and add magnetism? *Nano Lett.* **2019**, *19*, 4581–4587.
[102] Lewis, D. J.; Tedstone, A. A.; Zhong, X. L.; Lewis, E. A.; Rooney, A.; Savjani, N.; Brent, J. R.; Haigh, S. J.; Burke, M. G.; Muryn, C. A. et al. Thin films of molybdenum disulfide doped with chromium by aerosol-assisted chemical vapor deposition (AACVD). *Chem. Mater.* **2015**, *27*, 1367–1374.
[103] Jellinek, F. The structures of the chromium sulphides. *Acta Cryst.* **1957**, *10*, 620–628.
[104] Tedstone, A. A.; Lewis, D. J.; O'Brien, P. Synthesis, properties, and applications of transition metal-doped layered transition metal dichalcogenides. *Chem. Mater.* **2016**, *28*, 1965–1974.
[105] Liu, X. M.; Zhao, X.; Ma, X.; Wu, N. H.; Xin, Q. Q.; Wang, T. X. Effect of strain on electronic and magnetic properties of n-type Cr-doped WSe_2 monolayer. *Phys. E: Low-Dimens. Syst. Nanostruct.* **2017**, *87*, 6–9.
[106] Azcatl, A.; Qin, X. Y.; Prakash, A.; Zhang, C. X.; Cheng, L. X.; Wang, Q. X.; Lu, N.; Kim, M. J.; Kim, J.; Cho, K. et al. Covalent nitrogen doping and compressive strain in MoS_2 by remote N_2 plasma exposure. *Nano Lett.* **2016**, *16*, 5437–5443.
[107] Nipane, A.; Karmakar, D.; Kaushik, N.; Karande, S.; Lodha, S. Few-layer MoS_2 p-type devices enabled by selective doping using low energy phosphorus implantation. *ACS Nano* **2016**, *10*, 2128–2137.
[108] Yang, L. M.; Majumdar, K.; Liu, H.; Du, Y. C.; Wu, H.; Hatzistergos, M.; Hung, P. Y.; Tieckelmann, R.; Tsai, W.; Hobbs, C. et al. Chloride molecular doping technique on 2D materials: WS_2 and MoS_2. *Nano Lett.* **2014**, *14*, 6275–6280.
[109] Li, S. Y.; Chen, X. Q.; Liu, F. M.; Chen, Y. F.; Liu, B. Y.; Deng, W. J.; An, B. X.; Chu, F. H.; Zhang, G. Q.; Li, S. L. et al. Enhanced performance of a CVD MoS_2 photodetector by chemical *in situ* n-type doping. *ACS Appl. Mater. Interfaces* **2019**, *11*, 11636–11644.
[110] Gong, Y. J.; Liu, Z.; Lupini, A. R.; Shi, G.; Lin, J. H.; Najmaei, S.; Lin, Z.; Elías, A. L.; Berkdemir, A.; You, G. et al. Band gap engineering and layer-by-layer mapping of selenium-doped molybdenum disulfide. *Nano Lett.* **2014**, *14*, 442–449.
[111] Zheng, B. Y.; Ma, C.; Li, D.; Lan, J. Y.; Zhang, Z.; Sun, X. X.; Zheng, W. H.; Yang, T. F.; Zhu, C. G.; Ouyang, G. et al. Band alignment engineering in two-dimensional lateral heterostructures. *J. Am. Chem. Soc.* **2018**, *140*, 11193–11197.
[112] Li, P. L.; Cui, J.; Zhou, J. D.; Guo, D.; Zhao, Z. Z.; Yi, J.; Fan, J.; Ji, Z. Q.; Jing, X. N.; Qu, F. M. et al. Phase transition and superconductivity enhancement in Se-substituted $MoTe_2$ thin films. *Adv. Mater.* **2019**, *31*, 1904641.
[113] Pető, J.; Ollár, T.; Vancsó, P.; Popov, Z. I.; Magda, G. Z.; Dobrik, G.; Hwang, C.; Sorokin, P. B.; Tapasztó, L. Spontaneous doping of the basal plane of MoS_2 single layers through oxygen substitution under ambient conditions. *Nat. Chem.* **2018**, *10*, 1246–1251.
[114] Cao, Q.; Dai, Y. W.; Xu, J.; Chen, L.; Zhu, H.; Sun, Q. Q.; Zhang, D. W. Realizing stable p-type transporting in two-dimensional WS_2 films. *ACS Appl. Mater. Interfaces* **2017**, *9*, 18215–18221.
[115] Yang, Q.; Wang, Z. G.; Dong, L. C.; Zhao, W. B.; Jin, Y.; Fang, L.; Hu, B. S.; Dong, M. D. Activating MoS_2 with super-high nitrogen-doping concentration as efficient catalyst for hydrogen evolution reaction. *J. Phys. Chem. C* **2019**, *123*, 10917–10925.
[116] Conroy, L. E.; Park, K. C. Electrical properties of the group IV disulfides, titanium disulfide, zirconium disulfide, hafnium disulfide and tin disulfide. *Inorg. Chem.* **1968**, *7*, 459–463.
[117] Jin, Z. P.; Cai, Z.; Chen, X. S.; Wei, D. C. Abnormal n-type doping effect in nitrogen-doped tungsten diselenide prepared by moderate ammonia plasma treatment. *Nano Res.* **2018**, *11*, 4923–4930.
[118] Qin, S.; Lei, W. W.; Liu, D.; Chen, Y. *In-situ* and tunable nitrogen-doping of MoS_2 nanosheets. *Sci. Rep.* **2014**, *4*, 7582.
[119] Khosravi, A.; Addou, R.; Smyth, C. M.; Yue, R. Y.; Cormier, C. R.; Kim, J.; Hinkle, C. L.; Wallace, R. M. Covalent nitrogen doping in molecular beam epitaxy-grown and bulk WSe_2. *APL Mater.* **2018**, *6*, 026603.
[120] Li, H. L.; Duan, X. D.; Wu, X. P.; Zhuang, X. J.; Zhou, H.; Zhang, Q. L.; Zhu, X. L.; Hu, W.; Ren, P. Y.; Guo, P. F. et al. Growth of alloy $MoS_{2x}Se_{2(1-x)}$ nanosheets with fully tunable chemical compositions and optical properties. *J. Am. Chem. Soc.* **2014**, *136*, 3756–3759.

[121] Duan, X. D.; Wang, C.; Fan, Z.; Hao, G. L.; Kou, L. Z.; Halim, U.; Li, H. L.; Wu, X. P.; Wang, Y. C.; Jiang, J. H. et al. Synthesis of $WS_{2x}Se_{2-2x}$ alloy nanosheets with composition-tunable electronic properties. *Nano Lett*. **2016**, *16*, 264–269.

[122] Verzhbitskiy, I. A.; Voiry, D.; Chhowalla, M.; Eda, G. Disorder-driven two-dimensional quantum phase transitions in Li_xMoS_2. *2D Mater*. **2020**, *7*, 035013.

[123] Barja, S.; Refaely-Abramson, S.; Schuler, B.; Qiu, D. Y.; Pulkin, A.; Wickenburg, S.; Ryu, H.; Ugeda, M. M.; Kastl, C.; Chen, C. et al. Identifying substitutional oxygen as a prolific point defect in monolayer transition metal dichalcogenides. *Nat. Commun*. **2019**, *10*, 3382.

[124] Su, W. T.; Jin, L.; Qu, X. D.; Huo, D. X.; Yang, L. Defect passivation induced strong photoluminescence enhancement of rhombic monolayer MoS_2. *Phys. Chem. Chem. Phys*. **2016**, *18*, 14001–14006.

[125] Shu, H. B.; Li, Y. H.; Niu, X. H.; Wang, J. L. Greatly enhanced optical absorption of a defective MoS_2 monolayer through oxygen passivation. *ACS Appl. Mater. Interfaces* **2016**, *8*, 13150–13156.

[126] Komsa, H. P.; Kotakoski, J.; Kurasch, S.; Lehtinen, O.; Kaiser, U.; Krasheninnikov, A. V. Two-dimensional transition metal dichalcogenides under electron irradiation: Defect production and doping. *Phys. Rev. Lett*. **2012**, *109*, 035503.

[127] KC, S.; Longo, R. C.; Wallace, R. M.; Cho, K. Surface oxidation energetics and kinetics on MoS_2 monolayer. *J. Appl. Phys*. **2015**, *117*, 135301.

[128] Bollinger, M. V.; Lauritsen, J. V.; Jacobsen, K. W.; Nørskov, J. K.; Helveg, S.; Besenbacher, F. One-dimensional metallic edge states in MoS_2. *Phys. Rev. Lett*. **2001**, *87*, 196803.

[129] Hu, Z. L.; Avila, J.; Wang, X. Y.; Leong, J. F.; Zhang, Q.; Liu, Y. P.; Asensio, M. C.; Lu, J. P.; Carvalho, A.; Sow, C. H. et al. The role of oxygen atoms on excitons at the edges of monolayer WS_2. *Nano Lett*. **2019**, *19*, 4641–4650.

[130] Islam, M. R.; Kang, N.; Bhanu, U.; Paudel, H. P.; Erementchouk, M.; Tetard, L.; Leuenberger, M. N.; Khondaker, S. I. Tuning the electrical property via defect engineering of single layer MoS_2 by oxygen plasma. *Nanoscale* **2014**, *6*, 10033–10039.

[131] Kang, N.; Paudel, H. P.; Leuenberger, M. N.; Tetard, L.; Khondaker, S. I. Photoluminescence quenching in single-layer MoS_2 via oxygen plasma treatment. *J. Phys. Chem. C* **2014**, *118*, 21258–21263.

[132] Kim, S.; Choi, M. S.; Qu, D. S.; Ra, C. H.; Liu, X. C.; Kim, M.; Song, Y. J.; Yoo, W. J. Effects of plasma treatment on surface properties of ultrathin layered MoS_2. *2D Mater*. **2016**, *3*, 035002.

[133] Tian, X. Z.; Kim, D. S.; Yang, S. Z.; Ciccarino, C. J.; Gong, Y. J.; Yang, Y.; Yang, Y.; Duschatko, B.; Yuan, Y. K.; Ajayan, P. M. et al. Correlating the three-dimensional atomic defects and electronic properties of two-dimensional transition metal dichalcogenides. *Nat. Mater*. **2020**, *19*, 867–873.

[134] Bosman, M.; Keast, V. J.; García-Muñoz, J. L.; D'Alfonso, A. J.; Findlay, S. D.; Allen, L. J. Two-dimensional mapping of chemical information at atomic resolution. *Phys. Rev. Lett*. **2007**, *99*, 086102.

[135] Suenaga, K.; Koshino, M. Atom-by-atom spectroscopy at graphene edge. *Nature* **2010**, *468*, 1088–1090.

[136] Zribi, J.; Khalil, L.; Zheng, B. Y.; Avila, J.; Pierucci, D.; Brulé, T.; Chaste, J.; Lhuillier, E.; Asensio, M. C.; Pan, A. L. et al. Strong interlayer hybridization in the aligned SnS_2/WSe_2 hetero-bilayer structure. *npj 2D Mater. Appl*. **2019**, *3*, 27.

[137] Ponomarev, E.; Pásztor, Á.; Waelchli, A.; Scarfato, A.; Ubrig, N.; Renner, C.; Morpurgo, A. F. Hole transport in exfoliated monolayer MoS_2. *ACS Nano* **2018**, *12*, 2669–2676.

[138] Darlington, T. P.; Carmesin, C.; Florian, M.; Yanev, E.; Ajayi, O.; Ardelean, J.; Rhodes, D. A.; Ghiotto, A.; Krayev, A.; Watanabe, K. et al. Imaging strain-localized excitons in nanoscale bubbles of monolayer WSe_2 at room temperature. *Nat. Nanotechnol*., in press, DOI: 10.1038/s41565-020-0730-5.

[139] Schuler, B.; Cochrane, K. A.; Kastl, C.; Barnard, E.; Wong, E.; Borys, N.; Schwartzberg, A. M.; Ogletree, D. F.; de Abajo, F. J. G.; Weber-Bargioni, A. Electrically driven photon emission from individual atomic defects in monolayer WS_2. 2019, arXiv:1910.04612. arXiv.org e-Print archive. https://arxiv.org/abs/1910.04612 (accessed Oct 10, 2019).

[140] Patoka, P.; Ulrich, G.; Nguyen, A. E.; Bartels, L.; Dowben, P. A.; Turkowski, V.; Rahman, T. S.; Hermann, P.; Kästner, B.; Hoehl, A. et al. Nanoscale plasmonic phenomena in CVD-grown MoS_2 monolayer revealed by ultra-broadband synchrotron radiation based nano-FTIR spectroscopy and near-field microscopy. *Opt. Express* **2016**, *24*, 1154–1164.

[141] Spizzirri, P. G.; Fang, J. H.; Rubanov, S.; Gauja, E.; Prawer, S. Nano-Raman spectroscopy of silicon surfaces. 2010, arXiv:1002.2692. arXiv.org e-Print archive. https://arxiv.org/abs/1002.2692 (accessed Feb 13, 2010).

[142] Edelberg, D.; Rhodes, D.; Kerelsky, A.; Kim, B.; Wang, J.; Zangiabadi, A.; Kim, C.; Abhinandan, A.; Ardelean, J.; Scully, M. et al. Approaching the intrinsic limit in transition metal diselenides via point defect control. *Nano Lett*. **2019**, *19*, 4371–4379.

[143] Shree, S.; George, A.; Lehnert, T.; Neumann, C.; Benelajla, M.; Robert, C.; Marie, X.; Watanabe, K.; Taniguchi, T.; Kaiser, U. et al. High optical quality of MoS_2 monolayers grown by chemical vapor deposition. *2D Mater*. **2019**, *7*, 015011.

[144] Strauf, S.; Michler, P.; Klude, M.; Hommel, D.; Bacher, G.; Forchel, A. Quantum optical studies on individual acceptor bound excitons in a semiconductor. *Phys. Rev. Lett*. **2002**, *89*, 177403.

[145] Zheng, Y. J.; Chen, Y. F.; Huang, Y. L.; Gogoi, P. K.; Li, M. Y.; Li, L. J.; Trevisanutto, P. E.; Wang, Q. X.; Pennycook, S. J.; Wee, A. T. S. et al. Point defects and localized excitons in 2D WSe_2. *ACS Nano* **2019**, *13*, 6050–6059.

[146] Kita, T.; Wada, O. Bound exciton states of isoelectronic centers in GaAs: N grown by an atomically controlled doping technique. *Phys. Rev. B* **2006**, *74*, 035213.

[147] Gupta, S.; Yang, J. H.; Yakobson, B. I. Two-level quantum systems in two-dimensional materials for single photon emission. *Nano Lett*. **2018**, *19*, 408–414.

[148] Zhang, Q.; Ren, Z. M.; Wu, N.; Wang, W. J.; Gao, Y. J.; Zhang, Q. Q.; Shi, J.; Zhuang, L.; Sun, X. N.; Fu, L. Nitrogen-doping induces tunable magnetism in ReS_2. *npj 2D Mater. Appl*. **2018**, *2*, 22.

[149] Li, B.; Xing, T.; Zhong, M. Z.; Huang, L.; Lei, N.; Zhang, J.; Li, J. B.; Wei, Z. M. A two-dimensional Fe-doped SnS_2 magnetic semiconductor. *Nat. Commun*. **2017**, *8*, 1958.

[150] Singh, N.; Schwingenschlögl, U. Extended moment formation in monolayer WS_2 doped with 3d transition-metals. *ACS Appl. Mater. Interfaces* **2016**, *8*, 23886–23890.

[151] Ramasubramaniam, A.; Naveh, D. Mn-doped monolayer MoS_2: An atomically thin dilute magnetic semiconductor. *Phys. Rev. B* **2013**, *87*, 195201.

[152] Zhao, X.; Xia, C. X.; Dai, X. Q.; Wang, T. X.; Chen, P.; Tian, L. Electronic and magnetic properties of X-doped (X = Ni, Pd, Pt) WS_2 monolayer. *J. Magn. Magn. Mater*. **2016**, *414*, 45–48.

[153] Gao, Y. Q.; Ganguli, N.; Kelly, P. J. Itinerant ferromagnetism in p-doped monolayers of MoS_2. *Phys. Rev. B* **2019**, *99*, 220406.

[154] Wang, Z. X.; Zhao, X. X.; Yang, Y. K.; Qiao, L.; Lv, L.; Chen, Z.; Di, Z. F.; Ren, W.; Pennycook, S. J.; Zhou, J. D. et al. Phase-controlled synthesis of monolayer $W_{1-x}Re_xS_2$ alloy with improved photoresponse performance. *Small* **2020**, *16*, 2000852.

[155] Pandey, S. K.; Alsalman, H.; Azadani, J. G.; Izquierdo, N.; Low, T.; Campbell, S. A. Controlled p-type substitutional doping in large-area monolayer WSe_2 crystals grown by chemical vapor deposition. *Nanoscale* **2018**, *10*, 21374–21385.